Electronic ISSN: 1309-0267

I J E A S

International Journal of Engineering & Applied Sciences

IJEAS

Volume 13, Issue 3
2021

Published by Akdeniz University

Honorary Editors

(in alphabetical order)

Prof. Atluri, S.N.- University of California, Irvine-USA
Prof. Liew, K.M.- City University of Hong Kong-HONG KONG
Prof. Lim, C.W.- City University of Hong Kong-HONG KONG
Prof. Liu, G.R.- National University of Singapore- SINGAPORE
Prof. Nath, Y.- Indian Institute of Technology, INDIA
Prof. Omurtag, M.H. -ITU
Prof. Reddy, J.N.-Texas A& M University, USA
Prof. Saka, M.P.- University of Bahrain-BAHRAIN
Prof. Shen, H.S.- Shanghai Jiao Tong University, CHINA
Prof. Xiang, Y.- University of Western Sydney-AUSTRALİA
Prof. Wang, C.M.- National University of Singapore- SINGAPORE
Prof. Wei, G.W.- Michigan State University-USA

Editor in Chief:

Assoc. Prof. Ibrahim AYDOGDU -Akdeniz University *aydogdu@akdeniz.edu.tr*

Associate Editors:

R.A. Kadir MERCAN –Mehmet Akif Ersoy University *kmercan@mehmetakif.edu.tr*

Editorial Board

(The name listed below is not Alphabetical or any title scale)

Prof. Xinwei Wang -Nanjing University of Aeronautics and Astronautics

Asst. Prof. Francesco Tornabene -University of Bologna

Asst. Prof. Nicholas Fantuzzi -University of Bologna

Assoc. Prof. Keivan Kiani - K.N. Toosi University of Technology

Asst. Prof. Michele Bacciocchi -University of Bologna

Asst. Prof. Hamid M. Sedighi -Shahid Chamran University of Ahvaz

Prof. Yaghoub Tadi Beni -Shahrekord University

Prof. Raffaele Barretta -University of Naples Federico II

Prof. Meltem ASİLTÜRK -Akdeniz University *meltemasilturk@akdeniz.edu.tr*

Prof. Metin AYDOĞDU -Trakya University *metina@trakya.edu.tr*

Prof. Ayşe DALOĞLU - KTU *aysed@ktu.edu.tr*

Prof. Oğuzhan HASANÇEBİ - METU *oguzhan@metu.edu.tr*

Asst. Prof. Rana MUKHERJİ - The ICFAI University

Assoc. Prof. Baki ÖZTÜRK - Hacettepe University

Assoc. Prof. Yılmaz AKSU -Akdeniz University

Assoc. Prof. Hakan ERSOY- Akdeniz University

Assoc. Prof. Mustafa Özgür YAYLI -Uludağ University

Assoc. Prof. Selim L. SANİN - Hacettepe University

Asst. Prof. Engin EMSEN -Akdeniz University

Prof. Serkan DAĞ - METU

Prof. Ekrem TÜFEKÇİ - İTÜ

Abstracting & Indexing

IJEAS provides unique DOI link to every paper published.

Editorial Scope

The journal presents its readers with broad coverage across some branches of engineering and science of the latest development and application of new solution algorithms, artificial intelligent techniques innovative numerical methods and/or solution techniques directed at the utilization of computational methods in solid and nano-scaled mechanics.

International Journal of Engineering & Applied Sciences (IJEAS) is an Open Access Journal

International Journal of Engineering & Applied Sciences (IJEAS) publish original contributions on the following topics:

Numerical Methods in Solid Mechanics

Nanomechanic and applications

Microelectromechanical systems (MEMS)

Vibration Problems in Engineering

Higher order elasticity (Strain gradient, couple stress, surface elasticity, nonlocal elasticity) Applied Mathematics

IJEAS allows readers to read, download, copy, distribute, print, search, or link to the full texts of articles.

CC BY NC SA

CONTENTS

International Journal of Engineering & Applied Sciences (IJEAS)
Vol. 13, Issue 3 (2021) 79-92
http://dx.doi.org/10.24107/ijeas.996630
Int J Eng Appl Sci 13(3) (2021) 79-92

Effect of Seismic Isolation with Triple Friction Pendulum Isolator Device on Weight Optimization of Steel Plane Frames

Refik Burak Taymuş [a], İbrahim Aydoğdu [b]*

[a] Department of Civil Engineering, Van 100. Yıl University, Van, Turkey
[b] Department of Civil Engineering, Akdeniz University, Antalya, Turkey
[*]E-mail address: refikburaktaymus@yyu.edu.tr [a*], aydogdu@akdeniz.edu.tr [b]

ORCID numbers of authors:
0000-0002-1489-9307 [*], 0000-0002-8281-2365

Received date: 16.09.2021
Accepted date: 25.10.2021

Abstract

In the study, the weight efficiency of the Triple Friction Pendulum Bearing (TFP) Isolators is investigated on optimal weight of planar steel frames. For this investigation, an optimization program based on Artificial Bee Colony (ABC) algorithm have been developed for this study. In the design of steel frames, the structure should satisfy strength, inter-story drift, top-story drift and geometric requirements that are implemented from LRFD-AISC. For the research, 8 different planar frames were optimized as seismic-isolated and fixed-based, which were diversified according to story height and bracing. According to the results, the frames with TFP isolators, especially non-braced ones are a lot more advantageous regarding the optimal weight.

Keywords: Triple friction pendulum isolator, Planar steel frame, Bracing, Seismic-isolated, Artificial bee colony algorithm

1. Introduction

Minimizing the damaging effects of earthquakes on the structure is one of the most popular fields of study in structural engineering. Various structural design methods are used for this purpose. One of the methods is seismic isolation of the structures. Isolator devices increase the period of the superstructure and thus decrease the earthquake-resulted story drifts and ground accelerations acting to the floors, which means that earthquake-induced deformations are mitigated. On the other hand, it should also be considered that seismic isolation can have a reducing effect on the cost of the superstructure because it can allow the dimensions of the structural elements to be smaller than those of traditional design. To investigate this effect, it is necessary to conduct a comparative study of seismic-isolated structures and fixed-based structures in terms of cost. It is very difficult to make this comparison with conventional methods and does not give a realistic result. In this context, the metaheuristic optimization techniques are effective methods for realistic comparison. Metaheuristic optimization techniques with swarm intelligence present consistent solutions to complex optimization problems [1-6]. Swarm intelligence is based on the resolution of problems in nature as a swarm rather than as an individual. Metaheuristic optimization algorithms are created by simulating the behavior of the swarm while it is foraging. Many metaheuristic optimization algorithms such as Genetic algorithm, Archimedean optimization algorithm, and Crow search algorithm

© 2021 R.B. Taymus, İ. Aydoğdu published by International Journal of Engineering & Applied Sciences. This work is licensed under a Creative Commons Attribution-NonCommercial-ShareAlike 4.0 International License

have been developed and successfully applied to complex optimization problem so far, and artificial bee colony algorithm (ABC) is one of these algorithms. ABC algorithm which simulates the foraging behavior of honey bees, performed well in structural optimization problems for optimal sizing of truss and frame structures [7-8].

In literature, there are many optimization studies related to seismic isolated structures. Skandalos et al. [9] conducted a comparative optimization study in terms of seismic response on fixed-based, base-isolated, and inter-story isolated structures. Tsipianitis and Tsompanakis [10] tried to optimize the seismic response of a seismic-isolated liquid storage tank by using swarm intelligence algorithms and used single friction pendulum and triple friction pendulum isolators from sliding-based isolator devices. In the study, dimensional parameters of the isolator devices were also optimized as well as the seismic response of the superstructure. In a study conducted by Çerçevik et al. [11], isolator period and damping ratio of seismic isolation systems were optimally designed by using metaheuristic search methods in a way to minimize the roof acceleration. Peng et al. [12] optimized an adaptive sliding base isolation system to prevent possible failure of isolator devices during an extreme ground motion and thus to improve the seismic performance of structures. Rizzian et al. [13] presented a study on sizing optimization of seismic isolated reinforced concrete structures where optimum design main parameters were superstructure material cost, top floor displacement, and acceleration and it was revealed that when the cost of seismic isolator devices was considered, base isolation did not provide a cost advantage to the structure in total while it had positive effects in top floor response and acceleration. In a study that Jiang et al. [14] conducted, isolator devices used in seismic-isolated simply supported bridge model in the near-fault region was optimized by considering the pulse effect.

Related to the papers mentioned above, it can be commented that there are not enough studies to observe the effect of seismic isolation regarding the cost of the superstructure. In this context, this paper contributes to the literature. The paper presents a comparative study of cost optimization of base-isolated and fixed-base structure models. Accordingly, four different examples are designed: (i) 4-story 2D steel frame with braces, (ii) 4-floor 2D steel frame without braces, (iii) 8-floor 2D steel frame with braces, (iv) 8-floor 2D steel frame without braces. Each of the examples is handled as both seismic-isolated and fixed-based. Triple friction pendulum (TFP) isolator devices are used for seismic isolation of the models. All the models are optimized by using ABC algorithm and the results from seismic-isolated models are compared to those from fixed-based ones.

2. Optimum Design of Steel Plane Frames

To optimally design steel frames, it is necessary to select frame member sections from a suitable steel section list in a way to satisfy specified limitations and serviceability by considering that the main objective of the design is to minimize the material cost of the frame. It is well-known that the material cost of a superstructure is proportional to its weight. Thus, the main function of the design can be given as in Eq. (1) [7].

$$W\left(\vec{x}\right) = \sum_{r=1}^{NG} m_r \cdot \sum_{s=1}^{t_r} l_s \tag{1}$$

Here, $\vec{x}$, $W(\vec{x})$, m_r, t_r, NG, and I_s respectively refer to a vector of the sequence number of W-sections selected for member groups, the weight of frame as a function of the selected sections, unit weight of frame section to use for group r, total member number of group r, total group number of frame, and member length of the member of group r. In the design, three different constraints are applied: (i) strength constraints, (ii) lateral drift constraints, and (iii) geometric constraints. Firstly, strength constraints to be complied with for each element of the frame are as in Eq. (2) [7].

$$g_s\left(\vec{x}\right)=\begin{cases}\dfrac{P_u}{\phi P_n}+\dfrac{8}{9}\dfrac{M_u}{\phi_b M_n}-1\leq 0 & \text{if} \quad \dfrac{P_u}{\phi P_n}\geq 0.2\\ \dfrac{P_u}{2\phi P_n}+\dfrac{M_u}{\phi_b M_n}-1\leq 0 & \text{if} \quad \dfrac{P_u}{\phi P_n}<0.2\end{cases} \tag{2}$$

Here, M_n, M_u, P_n, and P_u respectively refer to, a nominal flexural strength of the frame, design moment, nominal axial strength, and design axial force for the structural element. M_u value is computed according to the second-order analysis of the structure. In the study, the approximate method specified in part C of the LRFD-AISC [15] specification was used for the second-order analysis.

Secondly, constraint functions of top and inter-story drift constraints are presented Eqs. (3)-(4) [7].

$$g_{id}\left(\vec{x}\right)=\frac{\Delta_{jl}^{str}}{h_{sx}\,/\,Ratio}-1\leq 0 \quad j=1,2,\ldots,n_{st} \quad l=1,2,\ldots,n_{lc} \tag{3}$$

$$g_{td}\left(\vec{x}\right)=\frac{\Delta_{jl}^{top}}{H\,/\,Ratio}-1\leq 0 \quad j=1,2,\ldots,n_{jtop} \quad l=1,2,\ldots,n_{lc} \tag{4}$$

Here, n_{lc}, H, n_{jtop}, Δ_{jl}^{top}, Δ_{jl}^{str}, n_{st}, h_{sx}, $Ratio$ are load-case number, height of frame, joint number of top story, j^{th} joint/l^{th} load-case top story displacement, j^{th} story/l^{th} load-case story drift, story number, story height, and lateral displacement limitation ratio from ASCE Ad Hoc Committee report [16]. This report has presented that lower and upper bounds of *Ratio* values are *1/750H* and *1/250H* for top story drift, and $1/500h_{sx}$ and $1/200h_{sx}$ for inter-story drift.

Finally, geometric constraints are explained in Eq. (5)-(6) [7].

$$g_{cc}\left(\vec{x}\right)=\sum_{i=1}^{n_{ccj}}\left(\frac{D_i^a}{D_i^b}-1\right)+\sum_{i=1}^{n_{ccj}}\left(\frac{m_i^a}{m_i^b}-1\right)\leq 0 \tag{5}$$

$$g_{bc}\left(\vec{x}\right)=\sum_{i=1}^{n_{j2}}\left(\frac{B_f^{bi}}{B_f^{ci}}-1\right)\leq 0 \tag{6}$$

Here, n_{ccj}, m_i^a, m_i^b, D_i^a, D_i^b, n_{j2}, D^{ci}, t_b^{ci}, B_f^{ci}, and B_f^{bi} respectively refer to unit weight of above story-W section, unit weight of below story-W section, depth of above story-W section, depth of below story-W section, number of beam-column connection joints, depth of column-W section at the joint *i*, flange thickness of column-W section at the joint *i*, flange width of column-W section at the joint *i*, flange width of column-W section at joint *i*, and flange width of beam-W section at the joint *i*. Fig. 1 describes these parameters.

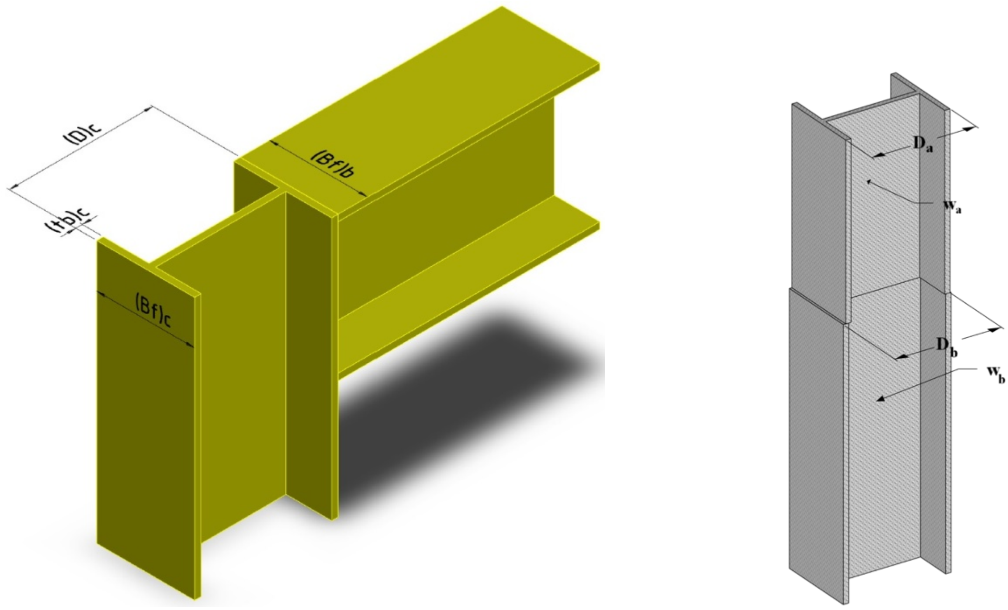

(a) (b)

Fig. 1. (a) Beam-Column, (b) Column-Column connections and constraint parameters

During the optimization process, if the candidate frame design does not satisfy Eq. (2)-(6), the weight of the structure design increases with the penalty function. The static penalty function (see Eq. (7)), which is frequently used in frame optimization problems, is preferred in the study.

$$W_p = W \cdot (1+P)^{\varepsilon} \tag{7}$$

Here, *Wp* is the penalized weight, *P* is the total penalty value and ε is the penalty coefficient ($\varepsilon = 2$ in this study). ε value was considered as 2 in [7] and this value was found to be effective. For this reason, it will be considered as ε=2 in this study. The value of *P* is calculated by Eq. (8) [7].

$$P = \sum_{i=1}^{NC} C_i \quad \text{and} \quad C_i = \begin{Bmatrix} 0 & \text{if} \quad g_i\left(\vec{x}\right) \le 0 \\ g_i\left(\vec{x}\right) & \text{if} \quad g_i\left(\vec{x}\right) > 0 \end{Bmatrix} \tag{8}$$

Here, subscript *i* represents any constraint function, NC is the total number of constraint functions in the optimization problem. In the study, the fitness value of the candidate solution (*Fit*) is inversely proportional to penalized weight and is formulated in Eq. (9).

$$Fit = \frac{1}{W_p} \tag{9}$$

3. Artificial Bee Colony (ABC) Algorithm

The ABC method was first developed by Karaboga and Basturk [17-23] by observing the behaviors of bees for minimum energy expenditure during foraging. The method categorizes worker bees as employed, onlooker, and scout bees. Employed bees handle collecting pollens from nectar sources (*NS'*s) and sharing information about *NS* with the colony. Onlooker bees decide to fly *NS* according to information shared from the employed bees. In the case of a depleted *NS*, scout bees look for new *NS* instead of depleted sources. In each cycle of the ABC, the employed bees choose one *NS*, and the onlooker bees have the same total number of flights as the worker bees. The scout bees replace the worker bee that flies to the depleted *NS*. Therefore, in the method, the numbers of employed bees, onlooker bees, and *NS* are equal. In the method, the *NS*, the location of the *NS*, and the quality of the *NS* represent the candidate solution, the design variables, and the fitness of the solution respectively. The optimization process of the ABC algorithm can be explained in these steps:

(i) The algorithm constitutes initial designs randomly by Eq. (10).

$$\vec{x}_{pi} = x_{li} + \alpha_p\left(\vec{x}_{ui} - \vec{x}_{li}\right) \quad \alpha_p \in [0,1] \quad i = 1,2,...,n \quad p = 1,2,...,pn \tag{10}$$

Here, α_p, n, pn is respectively a random value between 0 and 1, element number of solution vector, and the number of *NS*. $\vec{x}_{ui}$ and $\vec{x}_{li}$ are respectively upper and lower bounds of $\vec{x}_i$. The algorithm evaluates the initial design, finds their fitness values, and assigns the trial values to the initial design as zero. All these values are stored in the algorithm memory.

(ii) Worker bees modify designs in the memory as in Eq. (11).

$$\vec{x}_{pi} = \vec{x}_{pi} + \beta_p\left(\vec{x}_{pi} - \vec{x}_{ki}\right) \quad \beta_p \in [-1,1] \quad k \neq i \quad i = 1,2,...,n \tag{11}$$

Here, $\vec{x}_{ki}$ is a randomly selected NS and β_p is a random value between -1 and 1. Then the ABC computes the fitness values of the new designs and compares them with the old designs. The new design replaces the old one if the new designs have better fitness. Otherwise, the old solution stays in memory and its trial value increased by one. This process is named as "greedy selection".

(iii) Onlooker bees figure out the designs to modify based on the information received from the worker bees. This decision must be based on a probability value, named as PV_p, calculated by Eq. (12).

$$PV_p = \frac{Fit\left(x_p\right)}{\sum_{p=1}^{pn} Fit\left(x_p\right)} \tag{12}$$

After the decision, the algorithm performs the same procedures to decided designs as in the worker bee part.

(iv) If the trial number of the design is greater than the limit value defined at the beginning of the optimization process, scout bees step in. Scout bees remove the design from the memory and find the new design in the same way with step (i).
After step (iv), the algorithm completes one cycle and goes back to step (ii). The algorithm performs operations between steps (ii) and step (iv) until it reaches the maximum cycle number and/or function evaluation number.

4. The Design of Triple Friction Pendulum Bearing (TFP) Isolators

TFP isolators are a type of frictional-based seismic isolator devices and are commonly used in seismic isolation of structures (see Fig. (2)). They are composed of 5 components: (i) Top concave sliding plate (C_1), (ii) Bottom concave sliding plate (C_2), (iii) Top concave slider (C_3), (iv) Bottom concave slider (C_4), and (v) Inner articulated slider (C_5). Figure 2 describes TFP's components and parameters. For the concave surfaces, it must be $R_1 = R_4$ and $R_2 = R_3$ and likewise $d_1 = d_4$ and $d_2 = d_3$ for the displacement capacities. There are four frictional interaction surfaces between the components. The friction coefficients of the surfaces are μ_1, μ_2, μ_3, and μ_4, from the bottom to the top, respectively and generally $\mu_2 = \mu_3 < \mu_1 = \mu_4$ or $\mu_2 = \mu_3 < \mu_1 < \mu_4$. In this study, it is taken as $\mu_2 = \mu_3 < \mu_1 = \mu_4$.

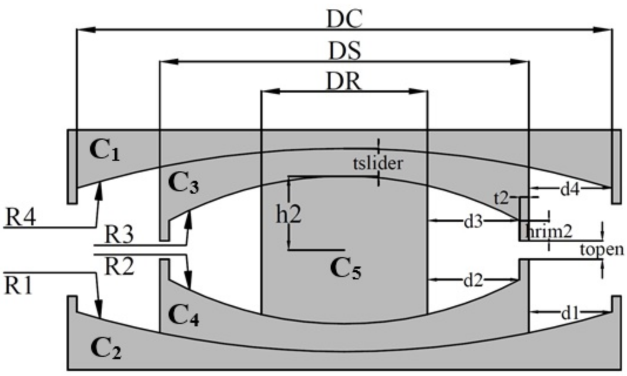

Fig. 2. A TFP model and its parameters

TFP isolator devices to use in this study are designed by abiding by "LRFD-Based Analysis and Design Procedures for Bridge Bearings and Seismic Isolators" [24]. *DC* and R_1 values required for the design are given in Table 1, quoting from section 4.4 of [24]. Considering the values selected from Table 1, d_1 and then *DS* can be calculated by Eq. (13)-(14).

$$d_1 = 0.15DC \tag{13}$$

$$DS = DC - 2d_1 \tag{14}$$

Table 1. R1 and DC parameter values of friction pendulum bearings [23]

R_1 (inch)	61	61	61	61	61	88	88	88	88	88	88	88	88	88
DC (inch)	14	18	22	31	36	27	31	36	39	41	44	46	51	56

After the calculation of *DS*, axial pressure, p_1, of a concave slider to concave sliding plate is obtained by Eq. (15).

$$p_1 = \frac{W}{\frac{\pi \cdot DS^2}{4}} \tag{15}$$

Here, *W* is an axial load on the isolator device and its unit must be *kips*. Friction coefficients are proportional to axial pressure and the μ_1 value is calculated by Eq. (16) as based on p_1.

$$\mu_1 = 0.122 - 0.01 p_1 \tag{16}$$

In this design, it is considered that the μ_1 value is better to be equal to 0.05 or larger than 0.05. If $\mu_1 < 0.05$, the above process must be repeated with new R_1 and *DC* values until $\mu_1 \geq 0.05$. Moreover, the μ_2 value is 30 percent of the μ_1 value. With the calculation of μ_2, if Eq. (16) is rearranged with respect to μ_2, Eq. (17) can be derived by subtracting p_2 from the new equation rearranged.

$$p_2 = \frac{0.122 - \mu_2}{0.01} \tag{17}$$

Here, p_2 is the axial pressure of the articulated slider to the concave slider. t_2, t_{slider}, and h_{rim2} parameters are obtained as respectively *DS/30*, *DS/7*, and *DS/20* for this study. In the next step, applying Eq. (15) for p_2, Eq. (18) is obtained.

$$p_2 = \frac{W}{\frac{\pi \cdot DR^2}{4}} \tag{18}$$

And thus, *DR* value can be attained by Eq. (19).

$$DR = \sqrt{\frac{4W}{\pi \cdot p_2}} \tag{19}$$

DR value is wished to be larger than *0.25DS* and smaller than *0.5DS*. If these boundary conditions exceed, all the processes must be repeated from the beginning. The calculation of *DR* value leads up to d_2 (See Eq. (20)).

$$d_2 = \frac{DS - DR - 2t_2}{2} \tag{20}$$

In the design, the distance between the closest endpoints of the support in the vertical direction is 1 inch. According to this, the h_2 value can be geometrically obtained by Eq. (21).

$$h_2 = R_2 - \sqrt{R_2^2 - \left(\frac{DS}{2} - t_2\right)^2} + h_{rim2} + \frac{t_{open}}{2} \tag{21}$$

Finally, h_1 value is calculated as related to h_2 and t_{slider} by Eq. (22).

$$h_1 = h_2 + t_{slider} \tag{22}$$

5. Design of Steel Plane Frames

This study aims to evaluate the effect of seismic isolation on weight by optimizing seismic isolated and fixed-based steel plane frame samples using the ABC optimization algorithm. For this goal, four steel plane frame examples, two of which have 4-story and the other two have 8-story, are designed. All 4-story and 8-story frames are modeled both with and without braces. Frame members are grouped as: one group for outer columns in every 4 floors, one group for inner columns in every 4 floors, one group for beams in every 4 floors, one group for braces in each floor. Joint, member, and group number of the frames are given in Table 2. The member grouping of all the frame examples are handled as both fixed-based and seismic-isolated (see Fig. (3-6)). The profiles to be assigned to the member groups are selected from the W sections from W150X13 to W920X1191 as given in LRFD-AISC. In seismic-isolated frames, 3 members are added to the base floor for 4-story frames and 5 members for 8-story frames to provide the lateral stability of isolator devices. The vertical loads applied to the frames are 2.88 kN/m^2 of dead load (D), 2.39 kN/m^2 of live load (L), and 0.755 kN/m^2 of snow load (S). The equivalent earthquake loads for each story are acted on both *X* and *Y* directions (EX and EY) and re-calculated in each iteration of the optimum design. The design load combinations are 1.4D, 1.2D + 1.6L + 0.5S, 1.2D + 0.5L + 1.6S, 1.2D + 0.5L +0.2S + 1.0EX, and 1.2D + 0.5L + 0.2S + 1.0EY. Top-story and inter-story drift limitations are taken as respectively $H / 300$ and $h_i / 300$, which H is the height of frame and h_i is the height of i^{th} story. The vertical loads, the drift limitations, and the load combinations are calculated by obeying to LRFD-AISC.

Table 2. Group and joint number of frame models

	4-Story Frame Models				8-Story Frame Models			
	FB		SI		FB		SI	
# of	WB	WOB	WB	WOB	WB	WOB	WB	WOB
Joint	24	20	24	20	70	54	70	54
Member	44	28	47	31	152	88	157	93
Group	7	3	7	3	14	6	14	6
WB: with braces WOB: without braces FB: Fixed-based SI: Seismic-isolated								

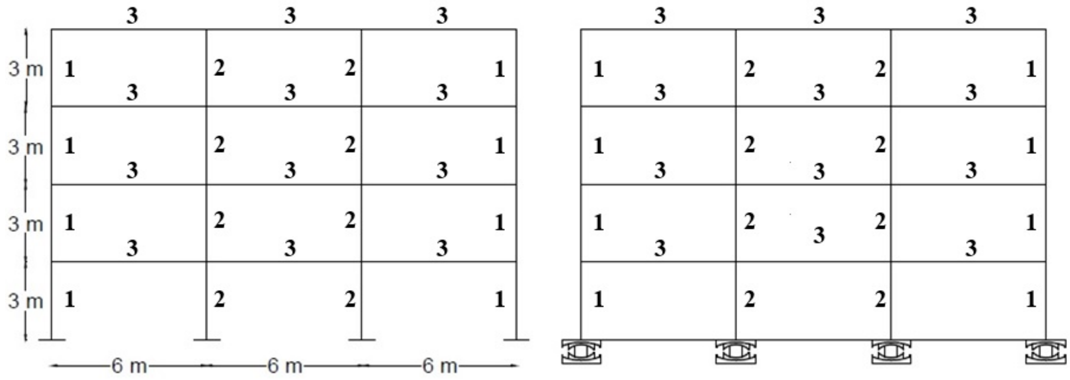

(a) (b)

Fig. 3. Element group number for (a) Fixed-Based, (b) Seismic-Isolated 4-Story Model without Braces

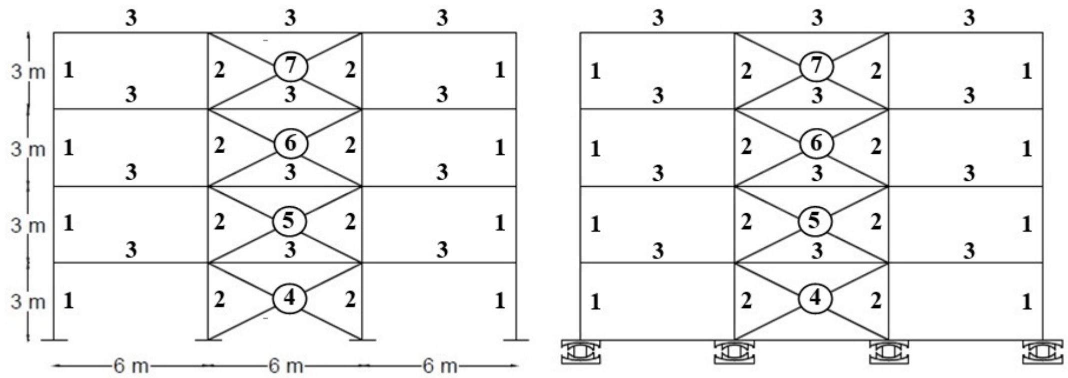

(a) (b)

Fig. 4. Element group number for (a) Fixed-Based, (b) Seismic-Isolated 4-Story Model with Braces

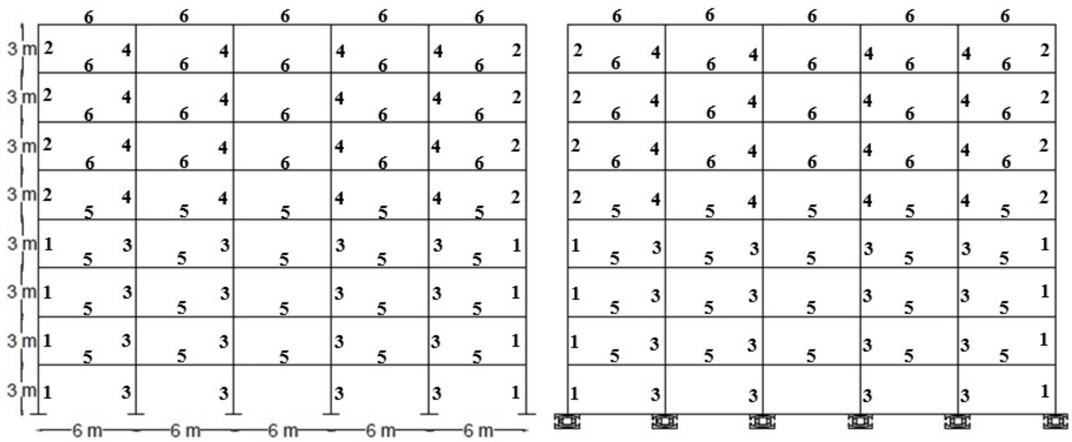

(a) (b)

Fig. 5. Element group number for (a) Fixed-Based, (b) Seismic-Isolated 8-Story Model without Braces

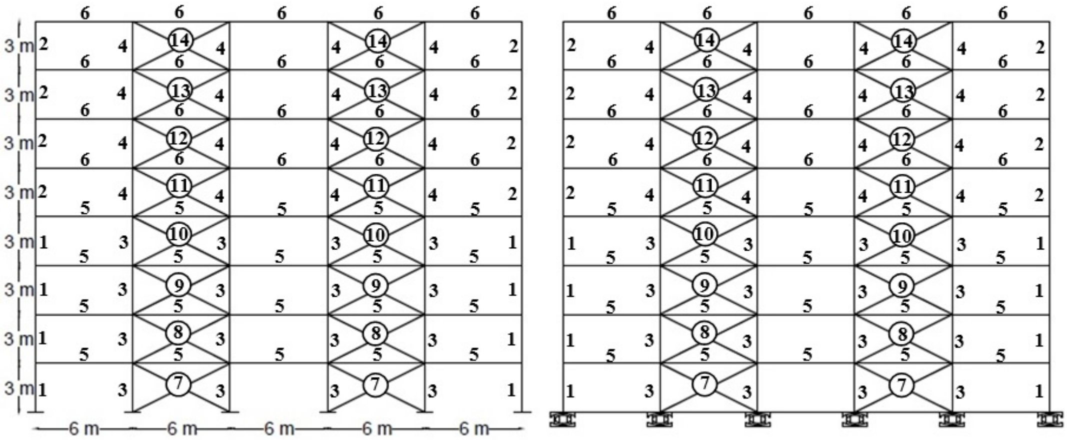
(a) (b)
Fig. 6. Element group number for (a) Fixed-Based, (b) Seismic-Isolated 8-Story Model with Braces

All the design examples are optimized by using ABC algorithm. Section lists of the optimum designs are given in Tables 3-6. Moreover, the maximum constraint values, which are minimum weight, PMM ratios, maximum story drifts, maximum total drifts, and maximum number of iterations, computed at optimized design for the design examples are presented in Table 7. Considering the weight values determined, it can be seen that the seismic isolation decreases the weight by: 28.45% for 4-story model without braces, 6.44% for 4-story model with braces, and 22.43% for 8-story without braces, 9.45% for 8-story model with braces. The design histories are shown in Fig. (7)-(10). It is clearly seen from the figures that ABC algorithm has sufficient convergence rate.

Table 3. The best design weights for 4-story frame models without braces

# of Group	Fixed-Based	Seismic-Isolated
1	W410X46.1	W250X17.9
2	W410X46.1	W310X32.7
3	W310X38.7	W250X32.7

Table 4. The best design weights for 4-story frame models with braces

# of Group	Fixed-Based	Seismic-Isolated
1	W150X22.5	W150X18
2	W200X31.3	W200X26.6
3	W130X23.8	W130X23.8
4	W200X19.3	W100X19.3
5	W150X18	W150X13
6	W150X13	W200X15
7	W150X13	W150X13.5

Table 5. The best design weights for 8-story frame models without braces

# of Group	Fixed-Based	Seismic-Isolated
1	W360X39	W460X52
2	W360X39	W250X28.4
3	W410X67	W410X60
4	W410X53	W310X32.7
5	W410X53	W310X44.5
6	W360X51	W250X32.7

Table 6. The best design weights for 8-story frame models with braces

# of Group	Fixed-Based	Seismic-Isolated
1	W200X26.6	W360X39
2	W200X22.5	W150X24
3	W460X74	W360X51
4	W360X39	W150X37.1
5	W150X22.5	W130X23.8
6	W200X26.6	W200X31.3
7	W250X32.7	W310X23.8
8	W150X29.8	W150X22.5
9	W310X38.7	W250X22.3
10	W310X32.7	W150X18
11	W150X29.8	W310X23.8
12	W200X26.6	W250X17.9
13	W150X13	W100X19.3
14	W310X21	W250X17.9

Table 7. Maximum constraint values computed at optimized design for design examples

	4-Story				8-Story			
	w Braces		w/o Braces		w Braces		w/o Braces	
	FB	SI	FB	SI	FB	SI	FB	SI
Minimum W (kN)	37.8	35.3	49.1	35.2	181.7	164.5	198.1	153.6
Max. story drift (mm)	3.6	1.2	9.6	9.6	7.4	4.8	8.1	9.1
Max. total drift (mm)	11.8	4	29.4	28.9	42.8	31.3	51.4	50.6
Max. PMM ratio	0.95	0.92	0.45	0.94	0.93	0.96	0.70	0.78
Max. iteration	1000	1000	1000	1000	1000	1000	1000	1000
w: with w/o: without FB: Fixed-based SI: Seismic-isolated								

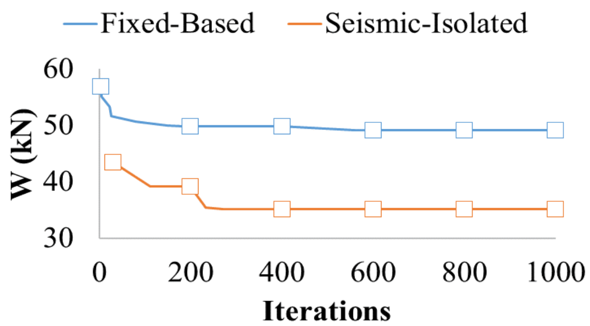

Fig. 7. Design histories of the ABC algorithm for 4-story frame without braces

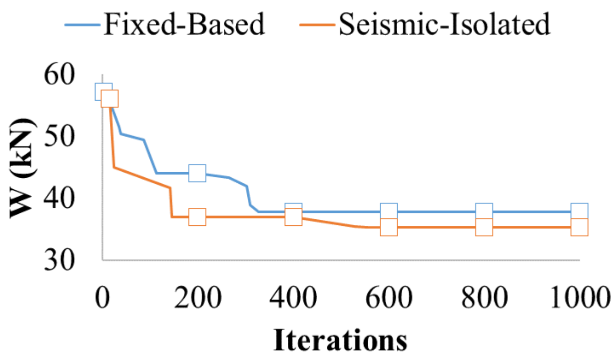

Fig. 8. Design histories of the ABC algorithm for 4-story frame with braces

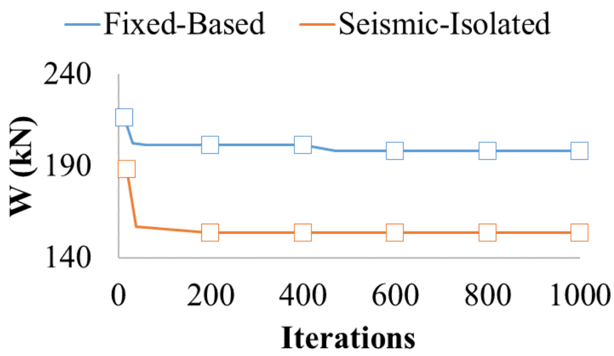

Fig. 9. Design histories of the ABC algorithm for 8-story frame without braces

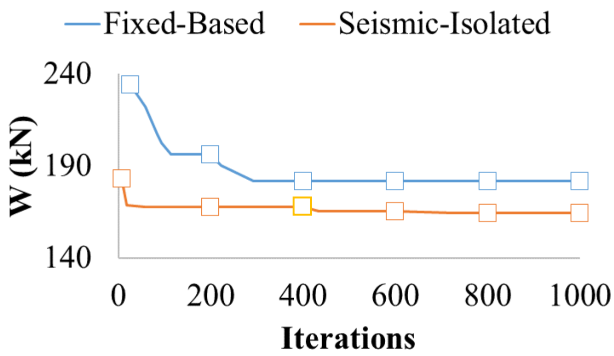

Fig. 10. Design histories of the ABC algorithm for 8-story frame with braces

6. Summary and Conclusions

To investigate the effect of seismic isolation on optimum weight of superstructures, 8 steel plane frame examples, which are considered as fixed-based and seismic-isolated, are tested. The frames are diversified as related to story height and bracing. TFP isolator devices are used for the seismic isolation. An optimization program developed as based on the ABC algorithm is employed to obtain the optimum structural weight values. The frame examples are designed in a way to satisfy strength, inter-story drift, top-story drift and geometric requirements that are implemented from LRFD-AISC. The following conclusions are drawn from the conducted study:

- The optimization program developed based on the ABC algorithm is well-performed with a consistent convergence rate and proximity to the limitations.
- For the examples with braces, the most effective design constraints are PMM ratios, while for the examples without braces, the most effective design constraints are story drift limitations.
- In the frame examples with braces, the drift values are far from the limit values. Therefore, the drift limitations are not very effective and the efficiency of the seismic isolation is not sufficient. On the other hand, the drift limitations are highly effective in the unbraced frame examples and the seismic isolation is very effective.
- It is observed that the weight advantage of the designs dominated by drift limitations is much higher than ones dominated by the PMM ratios.

- The seismic isolation offers more advantage in the unbraced frames rather than the braced ones in terms of the weight because drift limitations are more dominated than the other limitations in terms of weight reduction. Seismic isolation decreases story drift values of superstructure. Accordingly, seismic isolation is not so effective in braced frames because braces already restrict the story drifts of the structure so that the structure cannot approach the drift limits. Therefore the effect of drift is not seen for the optimum weight solution of seismic-isolated braced frames.

In the study, it is seen that the seismic isolation generally offers a weight advantage depending on the drift values, and it is understood that this advantage is much lower than the drift effect for the PMM values. However, the lateral drifts in irregular and 3-D structures result in undesirable effects such as torsion, and in these types of structures, the effect of seismic isolation on optimum design can be seen better. In the light of these assumptions, the effect of seismic isolation on the optimal design of 3-D structures is thought to be done in future studies. Although the design based on seismic isolation offers a cost advantage, this advantage can be lost when the cost of the isolator devices is taken into account. A more realistic comparison is made if the structure is optimized together with the cost of the isolator devices. Such a study is planned to be conducted in the future.

References

[1] Dillen, W., Lombaert, G., and Schevenels, M., A hybrid gradient-based/metaheuristic method for Eurocode-compliant size, shape and topology optimization of steel structures, *Engineering Structures*, 239, 112137, 2021.

[2] Ficarella, E., Lamberti, L., and Degertekin, S.O., Comparison of three novel hybrid metaheuristic algorithms for structural optimization problems, *Computers and Structures*, 244, 106395, 2021.

[3] Gonçalves, M.S., Lopez, R.H., and Fleck Fadel Miguel, L., Search group algorithm: A new metaheuristic method for the optimization of truss structures, *Computer and Structures*, 153, 165-184, 2015.

[4] Jahangiri, M., Hadianfard, M.A., Najafgholipour, M.A., Jahangiri, M., Gerami, M.R., Interactive autodidactic school: A new metaheuristic optimization algorithm for solving mathematical and structural design optimization problems, *Computer and Structures*, 235, 106268, 2020.

[5] Tran-Ngoc, H., Khatir, S., Ho-Khac, H., De Roeck, G., Bui-Tien, T., Abdel Wahab, M., Efficient Artificial neural networks based on a hybrid metaheuristic optimization algorithm for damage detection in laminated composite structures, *Composite Structures*, 262, 113339, 2021.

[6] Fleck Fadel Miguel, L., Fleck Fadel Miguel L., Shape and size optimization of truss structures considering dynamic constraints through modern metaheuristic algorithms, *Expert Systems with Applications*, 39, 9458-9467, 2012.

[7] Aydoğdu, İ., Akın, A., Saka, M.P., Design optimization of real world steel space frames using artificial bee colony algorithm with Levy flight distribution, *Advances in Engineering Software*, 92, 1-14, 2016.

[8] Jawad, F.K.J., Ozturk, C., Dansheng, W., Mahmood, M., Al-Azzawi, O., Al-Jemely, A., Sizing and layout optimization of truss structures with artificial bee colony algorithm, *Structures*, 30, 546-559, 2021.

[9] Skandalos, K., Afshari, H., Hare, W., Tesfamariam, S., Multi-objective optimization of inter-story isolated buildings using metaheuristic and derivative-free algorithms, *Soil Dynamics and Earthquake Engineering*, 132, 106058, 2020.

[10] Tsipianitis, A., Tsompanakis, Y., Optimizing the seismic response of base-isolated liquid storage tanks using swarm intelligence algorithms, *Computers and Structures*, 243, 106407, 2021.

[11] Çerçevik, A.E., Avşar, Ö., Hasançebi, O., Optimum design of seismic isolation systems using metaheuristic search methods, *Soil Dynamics and Earthquake Engineering*, 131, 106012, 2020.

[12] Peng, Y., Ma, Y., Huang, T., De Domenico, D., Reliability-based design optimization of adaptive sliding base isolation system for improving seismic performance of structures, *Reliability Engineering and System Safety*, 205, 107167, 2021.

[13] Rizzian, L., Leger, N., Marchi, M., Multiobjective sizing optimization of seismic-isolated reinforced concrete structures, *Procedia Engineering*, 199, 372-377, 2017.

[14] Jiang, L., Zhong, J., Yuan, W., The pulse effect on the isolation device optimization of simply supported bridges in near-fault regions, *Structures*, 27, 853-867, 2020.

[15] LRFD-AISC, Manual of steel construction, In: "Load and Resistance Factor Design", Third Edition, AISC, I&II, 2001.

[16] Ad Hoc Committee on Serviceability, Structural serviceability: A critical appraisal and research needs, *Journal of Structural Engineering, ASCE*, 112(12), 2646–2664, 1986.

[17] Karaboga, D., An idea based on honey bee swarm for numerical optimization, Technical Report-TR 06, 2005.

[18] Karaboga, D., Basturk, B., A powerful and efficient algorithm for numerical function optimization: artificial bee colony (ABC) algorithm, *Journal of Global Optimization*, 39, 459-471, 2007.

[19] Basturk, B., Karaboga, D., An artificial bee colony (ABC) algorithm for numeric function optimization, *Proceedings of IEEE Swarm Intelligence Symposium*, Indianapolis, Indiana, USA, 12–14 May 2006.

[20] Karaboga, D., Basturk, B., Artificial bee colony (ABC) optimization algorithm for solving constrained optimization problems, *IFSA 2007: Foundations of Fuzzy Logic and Soft Computing*, LNCS: 4529, 789–798, 2007.

[21] Karaboga, D., Basturk, B., On the performance of artificial bee colony (ABC) algorithm, *Applied Soft Computing*, 8(1), 687–697, 2008.

[22] Karaboga, D., Akay, B., A modified artificial bee colony (ABC) algorithm for constrained optimization problems, *Applied Soft Computing*, 11, 3021–3031, 2011.

[23] Karaboga, D., Gorkemli, B., Ozturk, C., Karaboga, N., A comprehensive survey: artificial bee colony (ABC) algorithm and applications. *Artificial Intelligence Review*, 42, 21–57, 2014.

[24] Constantinou, M.C., Kalpakidis, I., Filiatrault, A., Ecker Lay, R.A., LRFD-Based analysis and design procedures for bridge bearings and seismic isolators, Technical Report, 2010.

International Journal of Engineering & Applied Sciences (IJEAS)
Vol.13, Issue 3 (2021) 93-105
http://dx.doi.org/10.24107/ijeas.1002115
Int J Eng Appl Sci 13(3) (2021) 93-105

Investigation of the Consolidation Behavior of Soft Soil Improved with Vertical Drains by Finite Element Method

Recep Akan [a*], *Sedat Sert* [b]

[a] *Department of Civil Engineering, Faculty of Engineering, Suleyman Demirel University*
[b] *Department of Civil Engineering, Faculty of Engineering, Sakarya University*
[*] *E-mail address*: recepakan@hotmail.com [a*], sert@sakarya.edu.tr [b]

ORCID numbers of authors:
0000-0002-9277-1659 [a*], *0000-0002-4114-6132* [b]

Received date: 29.09.2021
Accepted date: 10.11.2021

Abstract

The primary consolidation may take long time due to the low permeability of clay soils in such cases soil improvement may be required to shorten the consolidation time, increase shear strength, and therefore bearing capacity. Preloading is one of the commonly used methods to consolidate soils before actual load and to strengthen weak compressible soils. In cases with time problems, the use of prefabricated vertical drains (PVD) with pre-loading shortens the drainage path and reduces the consolidation time by taking advantage of the horizontal permeability of the soils is generally higher. In this study, an embankment constructed at different load rates with constant accelerates and analyzes were performed for the non-drained and drained conditions of clay soils with PVDs are in 2m, 1m, and 0.5m intervals. In this way, the effect of load rate and PVD usage on consolidation settlement and excess pore pressures in underlying low permeable clayey soil was investigated.

Keywords: Embankment, Soft Clay, Consolidation, Load Rate, Prefabric Vertical Drain.

1. Introduction

Embankments on soft soils are one of the most common consolidation problems of soil mechanics. Primary consolidation can take a long time due to the low permeability of clay soils, and in such cases, soil improvement may be required to shorten the consolidation time and increase the shear strength and thus the bearing capacity [1]. Preloading is one of the most commonly used remediation techniques to consolidate soils and strengthen weakly compressible soils before the actual load acts. This method has been successfully applied in accelerating the settlement and strengthening of soft clays used for highway embankments, industrial and residential structures, and airport roads, and is quite suitable if sufficient time is available [2]. In cases where there is a time problem, this method can be used together with PVD, and the permeability of the soils can be greatly increased by taking advantage of the generally higher horizontal permeability and shortening the drainage length. The easy-to-manufacture PVD remediation method [3, 4] also reduces the consolidation time [1, 5–9] The theory of horizontal consolidation of vertical drains was first introduced by Barron [10] and has been modified by many researchers [11–14]. Hansbo [15] introduced the "unit cell" approach that takes into account the well resistance and the distortion effect, and then Hird et al. [16] formulated the two-dimensional planar strain situation. In addition, since the finite

© 2021 R. Akan, S. Sert published by International Journal of Engineering & Applied Sciences. This work is licensed under a Creative Commons Attribution-NonCommercial-ShareAlike 4.0 International License

element solution using planar strain became widespread, Indraratna and Redana [17] extended the equivalent unit cell theory to transform parameters such as permeability.

To check the accuracy of the results of the analysis given by the finite element software of the embankments made on soft soils, Borges [18] analyzed the real embankment model that is studied by Quaresma [19] and Yeo [20] by the finite element software and compared the analysis results with the real measurements in the field. Although the results were sufficiently consistent in terms of vertical settlements and excess pore pressures, they gave qualitatively similar but quantitatively different results in terms of horizontal displacements. Shen et al. [21] analyzed two different models, one improved by using PVD and the other without drain, with the help of an equivalent vertical permeability approach in order to examine the effect of using drains on soft soils. They placed PVDs at 1.5m intervals and 19 m lengths and revealed that the permeability of soft soils increased 30 times with the use of PVD, and excess pore damping could be accelerated. Chai et al. [22] and Ong and Chai [23] investigated the effect of surcharge loading speed on the vacuum preloading method. For this purpose, they performed a series of horizontal drain consolidation tests and triaxial tests in the laboratory, and as a result, they stated that loading at low velocities causes lower horizontal displacements. In addition to these studies, Chai and Rondonuwu [24] argued in their study that the optimum load rate increases with the increase of the initial effective stress of the soil. Lo et al. [25] supported a geogrid-reinforced road embankment with PVDs and examined the long-term performance of this embankment. The authors followed the tensile stresses in the geogrid and the excess pore pressure in the field for 400 days, followed by the settlements for 9 years. They tried to estimate the measured values using unit cell finite element analysis and compared the results with the actual values. As a result, it was revealed that the measured and predicted values of the excess pore pressures were compatible, and the estimated settlements for the center of the fill were smaller than the actual measured values. Akan et al. [26] investigated the effect of using PVD on the excess pore pressures, the damping times of these pressures, and the consolidation settlement of soft clay soils under different loading conditions. It was stated that lower excess pore pressures occur in the case with the drain and the damping times are reduced by 70-85% compared to the case without the drain, and the highest values are reached when the consolidation settlement is loaded at once without waiting for the embankment. Wang et al. [27] developed a model in the laboratory to evaluate the performance of the method in which vacuum and preload are used together and examined the effect of load rate by determining the horizontal displacements, vertical displacements, undrained shear strength, percentage of consolidation, horizontal consolidation coefficient and bearing capacity occurring on the ground at 3 different load rates. The findings of the research showed that the horizontal displacement is less in the fastest loading condition, the consolidation is completed faster and it gives higher bearing capacity values due to high final consolidation settlement. However, it is stated here that it should be taken into account that the vacuum pressure can reach different values for different load rates, and therefore the possibility that this situation may have affected the results should not be ignored. Kaisarta and Ilyas [28] aimed to obtain the settlement amount and time of consolidation of the soil during the vacuum process with the lateral distance between the vertical drains placed to accelerate the consolidation process and the damping of the excess pore pressure. For this purpose, they compared the settlement results obtained from a construction project with the results obtained from the finite element model created with the help of PLAXIS 2D. Similarly, Zhafirah et al. [29] performed analyzes with the analytical method to compare the consolidation time of soft soils before and after soil improvement using PVD. Nguyen et al. [30] discussed the necessity of using the latest analytical method and numerical simulation in a soil improvement project with vacuum PVD. For this purpose, a matching scheme is presented to derive suitable soil and drainage properties that are compatible with each other in analytical solution and numerical modeling. Nguyen et al. [31] have achieved a simple solution for vacuum preloaded PVDs that can be easily incorporated into the conventional method by applying the Laplace transform technique. Syahril [32] compared the results of the experimental and the numerical analysis with the finite element method. For this purpose, plate loading tests and two different consolidation tests were performed for with and without PVD soils in the laboratory, numerical analysis with the finite element method was carried out with the help of ETABS 2016 software. In addition, the finite element method is used to perform analysis in many different areas. For instance, Tigdemir et al. [33] present a numerical model for wheel-snow interaction using the finite element method. SolidWorks and ANSYS Design modeler are used to create a tire model for this purpose. The prepared models are analyzed using ANSYS Explicit Dynamics with the Mooney- Rivilin tire model. Yaylaci et al. [34] investigate the contact problem of an elastic layer resting on a rigid foundation. Two-dimensional analysis was carried out with the help of ANSYS, which is based on the Finite Element Method (FEM). Mercan and Civalek [35] present a fast and accurate method for determining the frequencies of microwires and nanowires, which are widely used in nanosensors, nanocircuits, and a variety of other scientific fields. COMSOL software is used to investigate the modal analysis of micro and nanowires. Thirty-nine modes are calculated to obtain the first ten-mode shapes and eigenfrequencies of silicon carbide nanowire. Figures captured from the software are used to present the results.

In the design of PVD, the PVD size will vary depending on the dimensions the manufacturer will provide and the time allowed for project completion. The required optimum spacing of PVDs should be chosen considering these variables, to meet the desired degree of consolidation within the allowable project time. For this purpose, it would be correct to decide to perform a series of analyzes with traditional methods or the finite element method. Within the scope of this paper, the variation of vertical and horizontal deformations, and the excess pore pressures during the construction of a road embankment with and without PVDs and at various load rates was investigated. The constructed models were analyzed with the help of the software of Plaxis 2D v20, which utilizes the finite element method, without PVD and PVDs with the 2m, 1m, and 0.5m intervals. Analysis results are presented in figures and discussed.

2. Material and Method

The soil layers are listed from top to bottom as Ground 1 (clay), Ground 2 (sand), Ground 3 (clay), and Ground 4 (sand), and their thicknesses are 6m, 2m, 5m, and 17m, respectively. The PVDs are 13m long and extend to the Ground 4 boundary (Fig. 1).

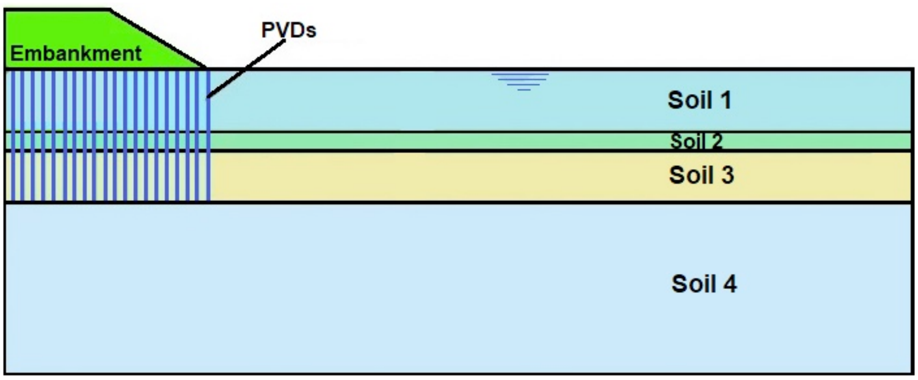

Fig. 1. Model and soil profile analyzed in Plaxis software

Soil 1 and Soil 3 are clay layers that have low permeability, while Ground 2 and Soil 4 are sand layers that have high permeability. Within the scope of the study, an embankment that has 6m of height was modeled in the Plaxis 2D v20 software, and analyzes were carried out at different load rates for different drain conditions to examine the effects of load rates and drain conditions on the consolidation behavior. Since the model is symmetrical, to reduce the analysis time, the system is divided into two parts from the center of symmetry and a solution is realized for just one part. The hardening soil model, which takes into account the assumption that the soil becomes stronger with the deformation, is preferred as the soil model. The developed model is presented in Fig. 1 and the parameters of the soil layers and embankment are shown in Table 1.

Plane strain was considered as the analysis model, and the model boundaries were 100m horizontally and 30m vertically. Analyzes were carried out as phased construction, the initial conditions were analyzed in the first step, and in the second step, the embankment has 6m of height was activated and consolidation analysis was conducted.

Table 1. Material properties of embankment and soil layers

	Soil 1 (clay)	**Soil 2**	**Soil 3 (clay)**	**Soil 4**	**Embankment**
Soil model	Hardening soil	Hardening soil	Hardening soil	Hardening soil	Hardening soil
Drainage type	Undrained(A)	Drained	Undrained(A)	Drained	Drained
γ_{unsat}**(kN/m^3)**	18	18	18	17	19
γ_{sat}**(kN/m^3)**	20	20	19	18	20
E_{50}^{ref} **(kN/m^2)**	3000	30000	12000	40000	30000
c'ref (kN/m^2)	5	0.1	20	1	5
ϕ′ref (°)	25	37	28	38	40
Ψ(°)	0	7	0	8	10
k_x **(m/day)**	8.64E-6	17.28	86.4E-6	8.64	1.4
k_y **(m/day)**	8.64E-6	17.28	86.4E-6	8.64	1.4
K_0	Automatic	Automatic	Automatic	Automatic	Automatic
OCR	1.8	2.0	1.6	1.6	2.0

3. Discussion

The road embankment has 6m of height is completed at different durations at a constant rate and the excess pore pressures that occur during the loading are shown in graphs for the cases without PVD and with PVDs with 2m, 1m, and 0.5m of intervals (Figs. 2-5).

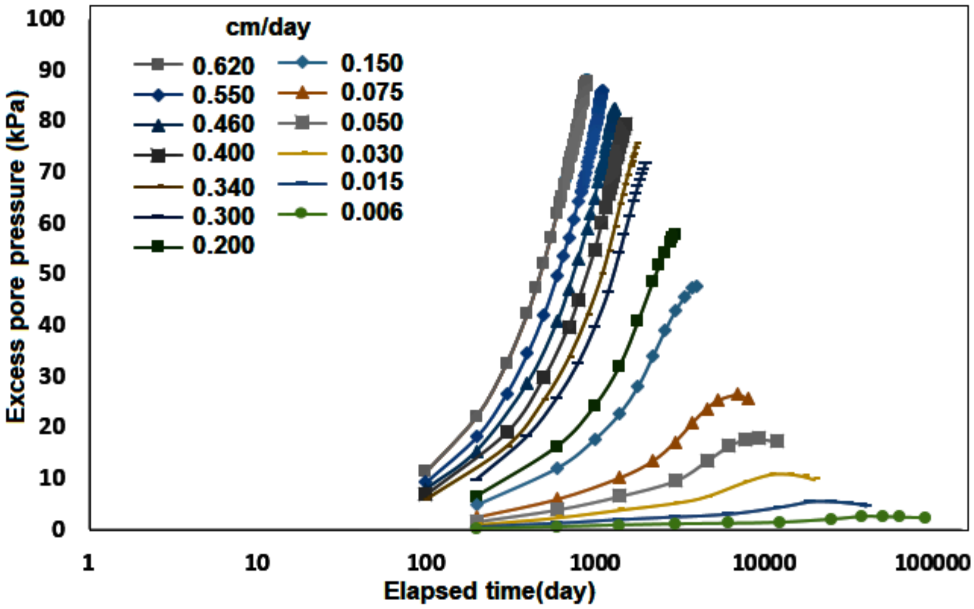

Fig. 2. Variations in the excess pore pressures below the embankment at different load rates in the case of the absence of PVD

In the case of without PVD, the excess pore pressure increases continuously till the end of the construction at load rates are more than 0.075 cm/day. In the cases that have load rates are less than 0.075 cm/day excess pore pressures increase in the first part but after a point, it starts to dampen.

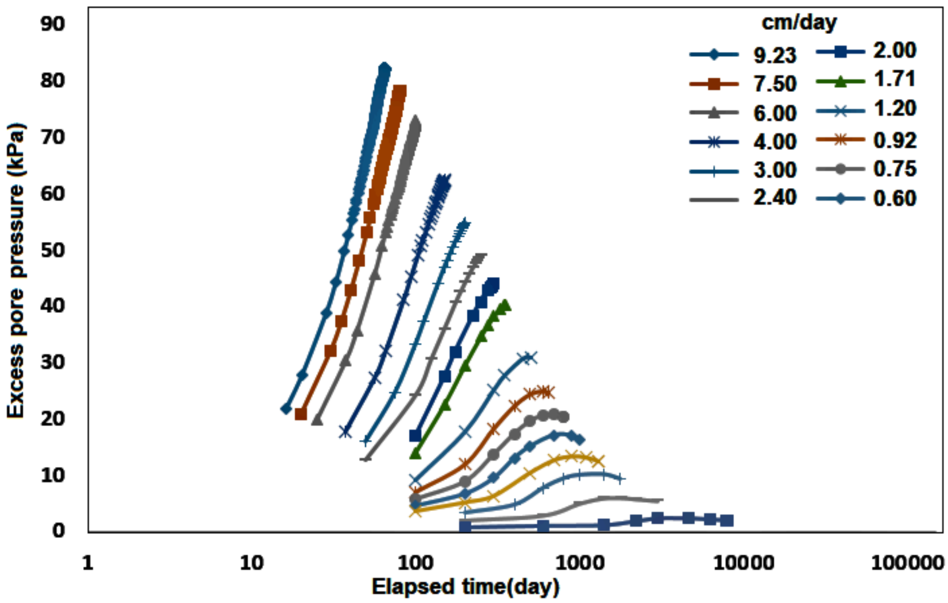

Fig. 3. Variations in the excess pore pressures below the embankment at different load rates in the case of PVDs with 2m intervals

In the case of with PVDs with 2m of intervals, the excess pore pressure increases continuously till the end of the construction at load rates are more than 0.92 cm/day. In the cases that have load rates are less than 0.92 cm/day excess pore pressures increase in the first part but after a point, it starts to dampen.

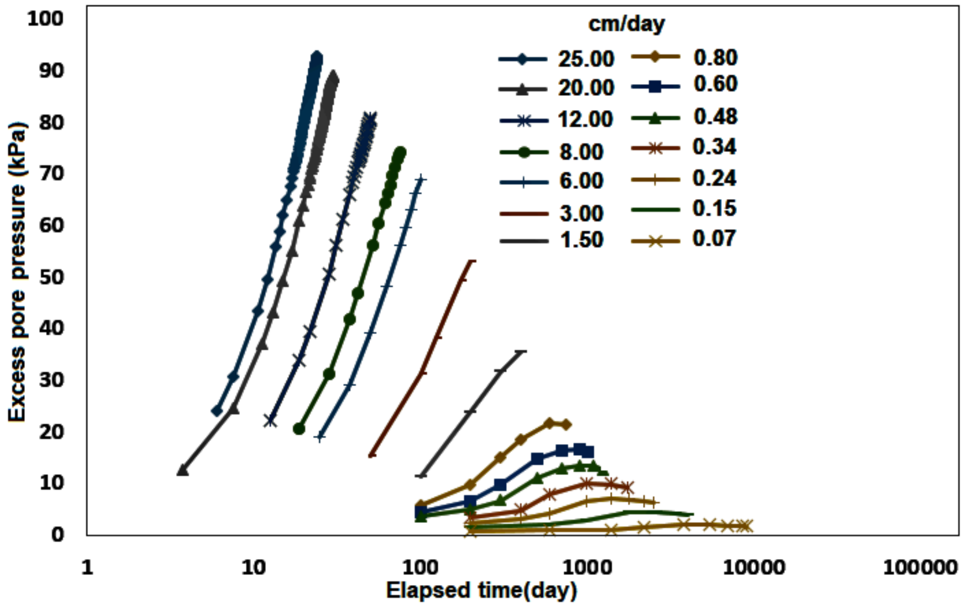

Fig. 4. Variations in the excess pore pressures below the embankment at different load rates in the case of PVDs with 1m intervals

In the case of with PVDs with 1m of intervals, the excess pore pressure increases continuously till the end of the construction at load rates are more than 0.8 cm/day. In the cases that have load rates are less than 0.8 cm/day excess pore pressures increase in the first part but after a point, it starts to dampen.

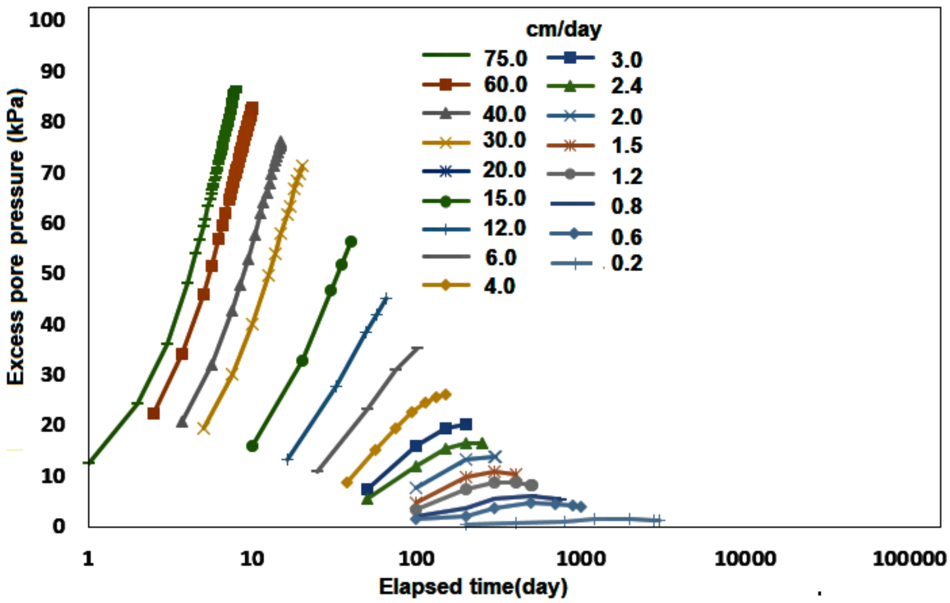

Fig. 5. Variations in the excess pore pressures below the embankment at different load rates in the case of PVDs with 0.5m intervals

In the case of with PVDs with 0.5m of intervals, the excess pore pressure increases continuously till the end of the construction at load rates are more than 2.4 cm/day. In the cases that have load rates are less than 2.4 cm/day excess pore pressures increase in the first part but after a point, it starts to dampen.

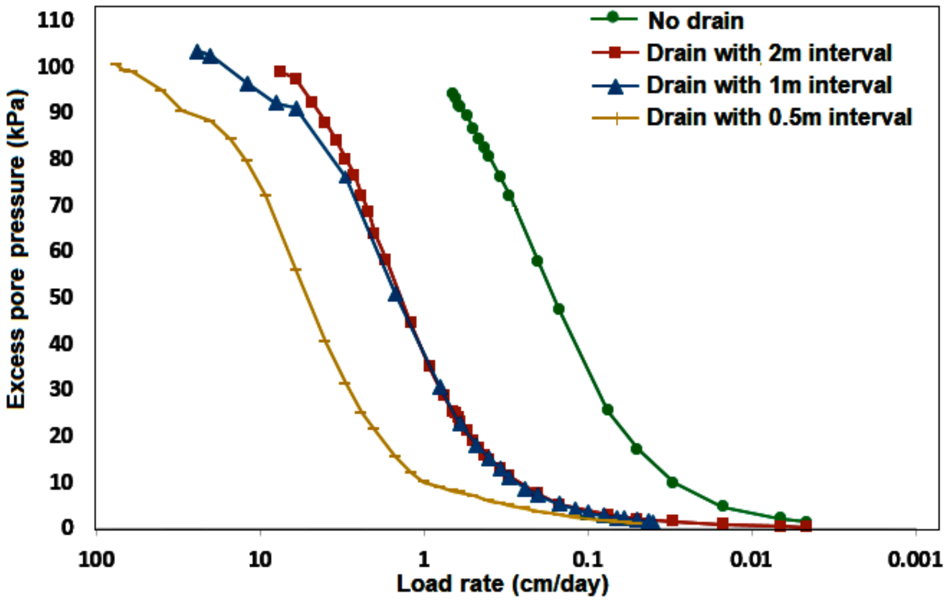

Fig. 6. The maximum excess pore pressure varies depending on the drain condition and load rate.

Maximum excess pore pressures for the cases that are with and without PVDs decrease with increasing load rates. It is observed that the behavior of the change in the excess pore pressure is similar, but similar excess pore pressures occur at, approximately 8 times for the case of 1m and 2m intervals of PVDs, and about 30 times for the case of 0.5m intervals of PVDs, faster load rates compared to the case without PVD (Fig. 6).

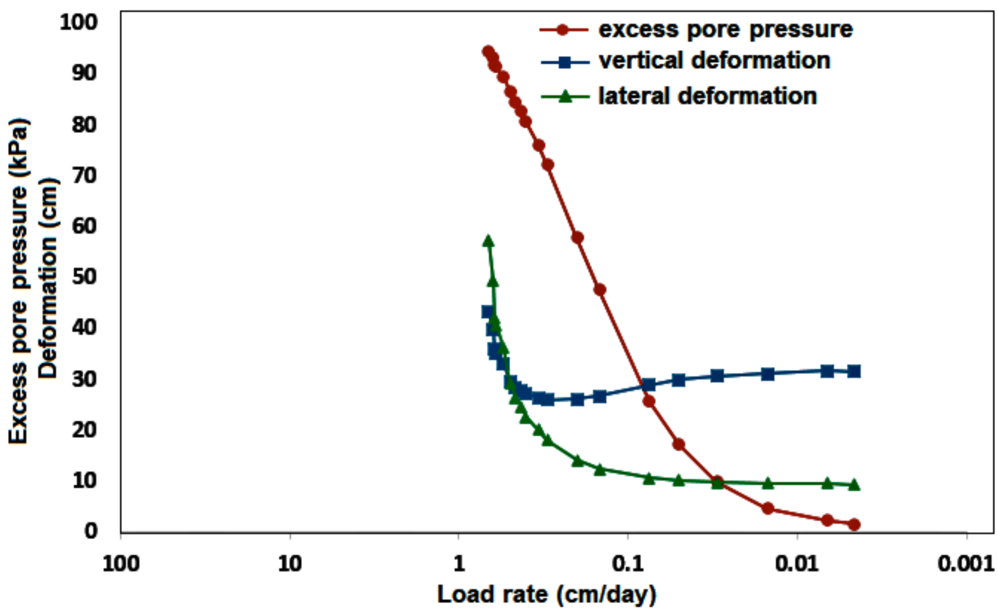

Fig. 7. In the absence of PVD, variations in the excess pore pressure, vertical and horizontal deformations are seen at various load rates.

The maximum horizontal and vertical deformations belonging to each case have different load rates are presented below as graphics (Figs. 7-10). The minimum vertical deformation in the condition that has no PVD is 26cm and the horizontal deformation is around 10cm. The minimum vertical deformation occurs at the load rate of 0.3 cm/day, and the minimum horizontal deformation occurs at the load rate of 0.08 cm/day.

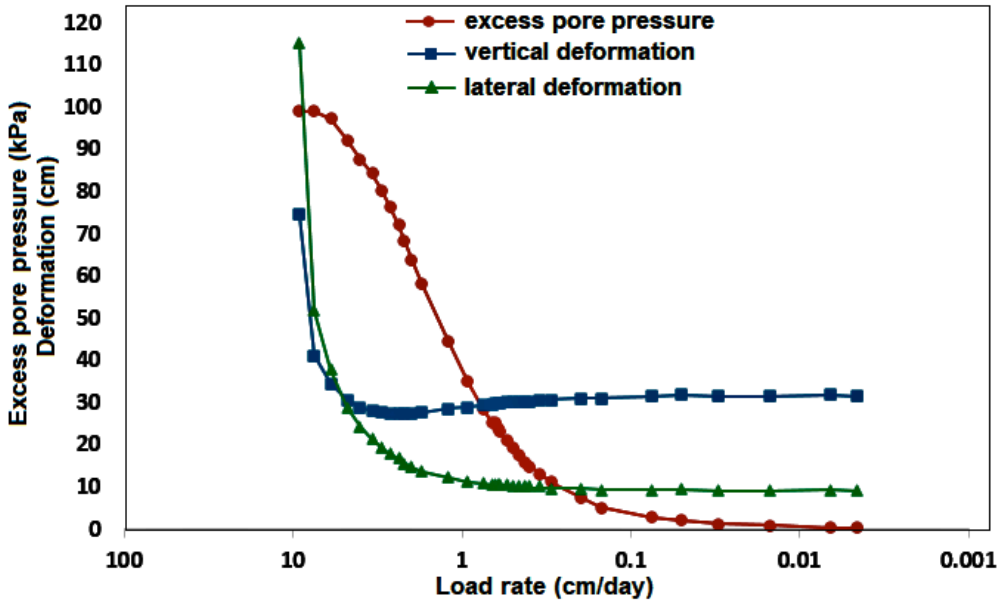

Fig. 8. Variations in the excess pore pressure, vertical and horizontal deformations in the case of PVDs with 2m intervals at varied load rates

The minimum vertical deformation that occurs in the case of drains with 2m intervals is 27cm and the horizontal deformation is around 10cm. The minimum vertical deformation occurs at the load rate of 2.4 cm/day, and the minimum horizontal deformation occurs at the load rate of 0.75 cm/day.

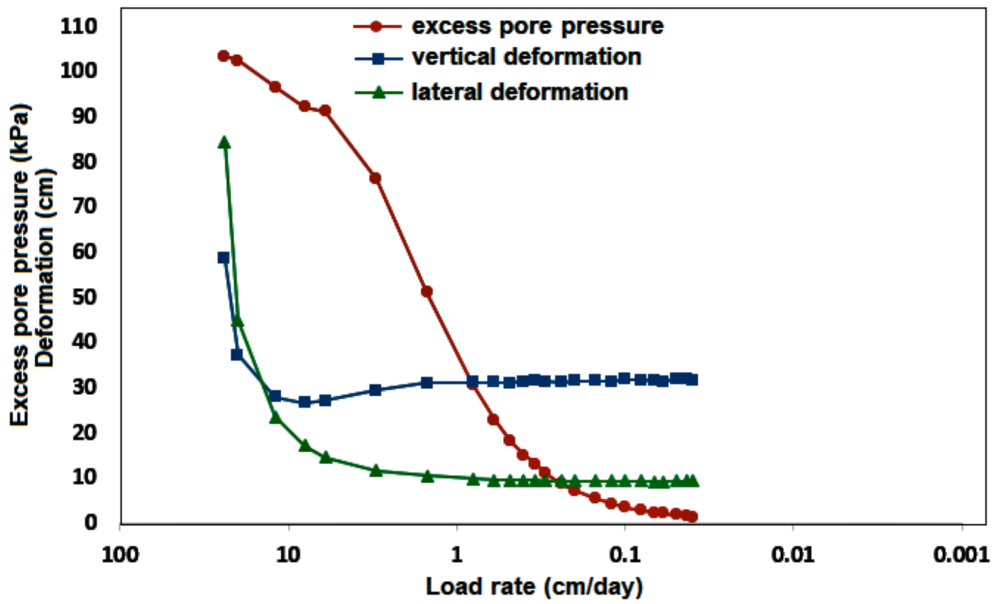

Fig. 9. Variations in the excess pore pressure, vertical and horizontal deformations in the case of PVDs with 1m intervals at varied load rates

The minimum vertical deformation that occurs in the case of drains with 1m intervals is 26cm and the horizontal deformation is around 10cm. The minimum vertical deformation occurs at the load rate of 8 cm/day, and the minimum horizontal deformation occurs at the load rate of 1.5 cm/day.

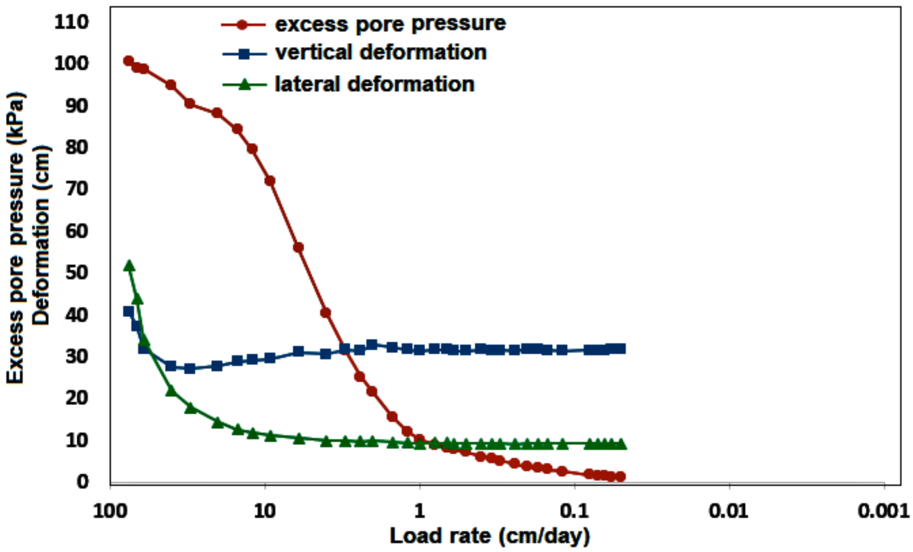

Fig. 10. Variations in the excess pore pressure, vertical and horizontal deformations in the case of PVDs with 0.5m intervals at varied load rates

The minimum vertical deformation that occurs in the case of drains with 0.5m intervals is 27cm and the horizontal deformation is around 10cm. The minimum vertical deformation occurs at the load rate of 30 cm/day, and the minimum horizontal deformation occurs at the load rate of 6 cm/day.

The maximum excess pore pressure decreases with the decrease of the load rate in both cases with and without PVD. Maximum horizontal and vertical deformations, decrease with the decrease in load rate to a limit but do not continue to decrease in slower load rates and remain almost constant.

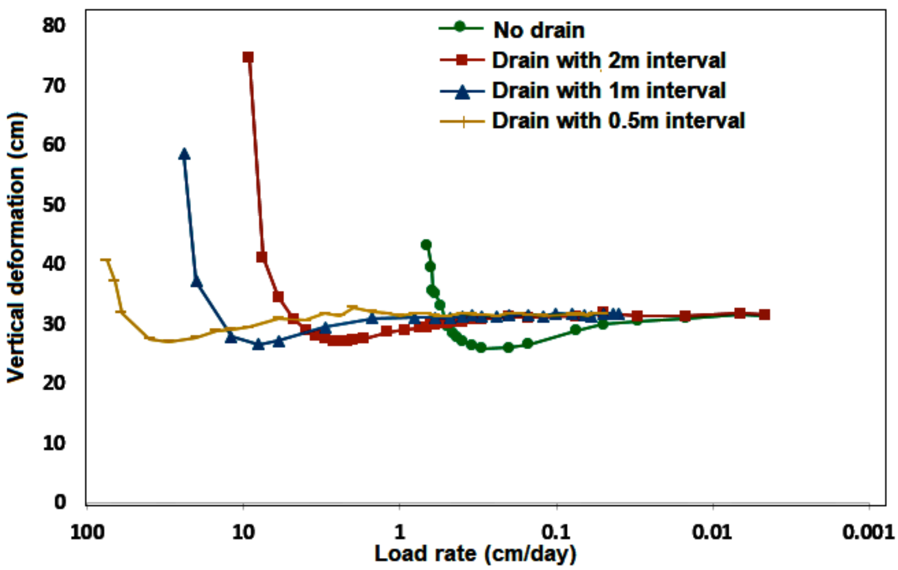

Fig. 11. Maximum vertical deformations in different drain conditions and at various load rates

Maximum vertical deformations occur in cases with different drain conditions that are similar in behavior and the minimum vertical deformations that occur for conditions with or without PVD is around 26 cm. It is seen that the load rates that cause minimum vertical deformation are 8, 27, and 100 times faster in the situations with PVDs with 2m, 1m, and 0.5m of intervals compared to the situation without PVD, respectively (Fig. 11).

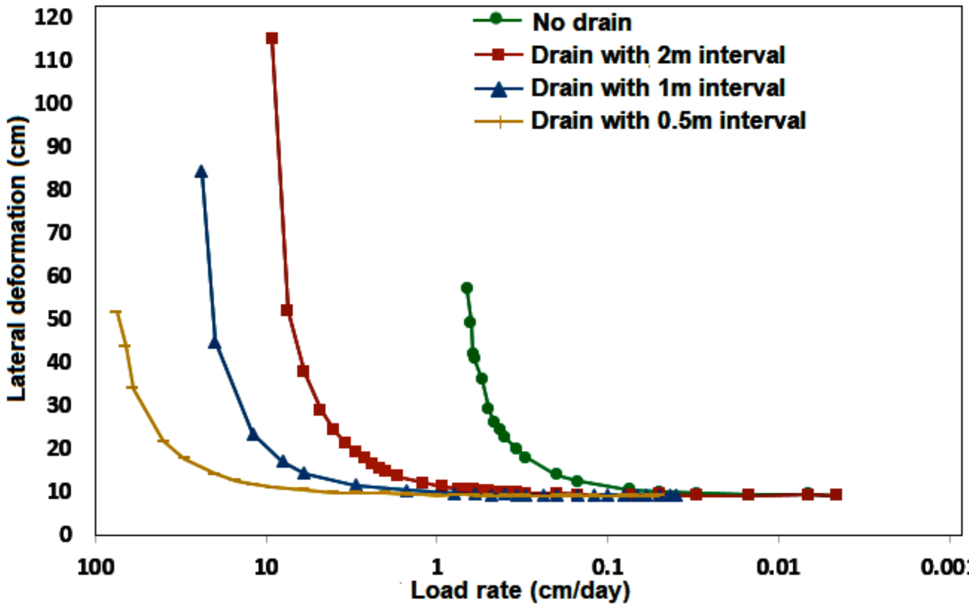

Fig. 12. Maximum lateral deformations in different drain conditions and at various load rates

Maximum lateral deformations occur in cases with different drain conditions that are similar in behavior and the minimum lateral deformations that occur for conditions with or without PVD is around 10cm. It is seen that the load rates that cause minimum lateral deformation are 9, 19, and 75 times faster in the situations with PVDs with 2m, 1m, and 0.5m of intervals compared to the situation without PVD, respectively (Fig. 12).

4. Conclusions

Within the scope of the study, excess pore pressures and deformations that will occur in the clay soil layers due to the filling sitting on the soil section containing low permeability clay soils were investigated. In this context, an embankment model with a height of 6 m has been analyzed for different vertical drain spacing situations and at different constant speeds, where the 6 m loading will be completed at different times. The effects of loading speed, vertical drain usage, and spacing on consolidation speed, deformations, and excess pore pressures were investigated as a result of the analyzes performed in the cases without PVD, and with PVDs having 2m, 1m, and 0.5m of intervals. The following results have been achieved:

- Maximum excess pore pressures, vertical deformations, and horizontal deformations that occur as a result of the embankment load at different rates are similar in behavior.

- Both with and without PVDs, the maximum excess pore pressures decrease with the increase in load rate.

- Maximum lateral and vertical deformations, decrease with the decrease in load rate to a limit but do not continue to decrease in slower load rates and remain almost constant.

- The minimum vertical deformations and lateral occur for conditions with or without PVD is around 26 cm and 10cm, respectively.

- Similar maximum excess pore pressures occur at, approximately 8 times for the case of 1m and 2m intervals of PVDs, and about 30 times for the case of 0.5m intervals of PVDs, faster load rates compared to the case without PVD.

- The load rates that cause minimum vertical deformation are 8, 27, and 100 times faster in the situations with PVDs with 2m, 1m, and 0.5m of intervals compared to the situation without PVD, respectively.

- The load rates that cause minimum lateral deformation are 9, 19, and 75 times faster in the situations with PVDs with 2m, 1m, and 0.5m of intervals compared to the situation without PVD, respectively.

References

[1] Zhou, W., Hong, H. P., & Shang, J. Q., Probabilistic design method of prefabricated vertical drains for soil improvement. *Journal of Geotechnical and Geoenvironmental Engineering*, 125(8), 659–664, 1999.

[2] Mitchell, J. K., Soil Improvement — State-of-the Art Report, *10th International Conference on Soil Mechanics and Foundation Engineering*, 4, 509–565, 1981.

[3] Shang, J. Q., Tang, M., & Miao, Z., Vacuum preloading consolidation of reclaimed land: a case study. *Canadian Geotechnical Journal*, 35(5), 740–749, 1998.

[4] Yan, S.-W., & Chu, J., Soil improvement for a storage yard using the combined vacuum and fill preloading method. *Canadian Geotechnical Journal*, 42(4), 1094–1104, 2011.

[5] Jamiolkowski, M., Lancellotta, R., & Wolski, W., Pre-compression and Speeding up Consolidation, General Report, *In Proceedings of Eight European Conference on Soil Mechanics and Foundation Engineering*, 1201–1226, Balkema, Rotterdam, 1983.

[6] Bergado, D. T., Anderson, L. R., Miura, N., & Balasubramaniam, A. S., Soft Ground Improvement, in Lowland and other Environments. ASCE Press, 1996.

[7] Rixner, J. J., Kraemer, S. R., & Smith, A. D., Prefabricated vertical drains, Engineering Guidelines, Final Report, 1, Washington DC, 1986.

[8] Holtz, R. D., Shang, J. Q., & Bergado, D. T., *Soil improvement*, Geotechnical and Geoenvironmental Engineering Handbook, Kluwer Academic Publishing, Norwell, USA, 2001.

[9] Chai, J. C., Miura, N., Zhu, H. H., & Yudhbir, A., Compression and consolidation characteristics of structured natural clay. *Canadian Geotechnical Journal*, 41(6), 1250–1258, 2004.

[10] Barron, R. A., Consolidation of fine-grained soils by drain wells by drain wells. *Transactions of the American Society of Civil Engineers*, 113(1), 718–742, 1948.

[11] Kjellman, W., Consolidation of clay soil by means of atmospheric pressure, *Proc. Conf. on Soil Stabilization*, M. I. T., 258–263, 1952. https://ci.nii.ac.jp/naid/10008001454. Accessed 20 September 2021

[12] Yoshikuni, H., & Nakanodo, H., Consolidation of soils by vertical drain wells with finite permeability. *Soils and Foundations*, 14(2), 35–46, 1974.

[13] Onoue, A., Consolidation by vertical drains taking well resistance and smear into consideration. *Soils and Foundations*, 28(4), 165–174, 1988.

[14] Zeng, G. X., & Xie, K. H., New development of the vertical drain theories, *In 12th Int. Conf. on Soil Mechanics and Foundation Engineering*, 1435–1438, Rotterdam, The Netherlands, 1989.

[15] Hansbo, S., Consolidation of Fine-grained Soils by Prefabricated Drains, *In Proceedings of the Tenth International Conference on Soil Mechanics and Foundation Engineering*, 677–682, Stockholm, 1981.

[16] Hird, C. C., Pyrah, I. C., & Russell, D., Finite element modelling of vertical drains beneath embankments on soft ground. *Geotechnique*, 42(3), 499–511, 1992.

[17] Indraratna, B., & Redana, I. W., Plane-Strain modeling of smear effects associated with vertical drains. *Journal of Geotechnical and Geoenvironmental Engineering*, 123(5), 474–478, 1997.

[18] Borges, J. L., *Geosynthetic-reinforced embankments on soft soils. Analysis and design,* University of Porto, 1995.

[19] Quaresma, M. G., *Behaviour and modelling of an embankment over soft soils reinforced by geotextile*, Universite Joseph Fourier, Grenoble I, 1992.

[20] Yeo, K. C., Simplified foundation data to predictors, *In Proceedings of the prediction symposium on a reinforced embankment on soft ground*, King's College, London, UK, 1986.

[21] Shen, S. L., Chai, J. C., Hong, Z. S., & Cai, F. X., Analysis of field performance of embankments on soft clay deposit with and without PVD-improvement. *Geotextiles and Geomembranes*, 23(6), 463–485, 2005.

[22] Chai, J. C., Carter, J. P., & Hayashi, S., Vacuum consolidation and its combination with embankment loading. *Canadian Geotechnical Journal*, 43(10), 985–996, 2006.

[23] Ong, C.-Y., & Chai, J.-C., Lateral displacement of soft ground under vacuum pressure and surcharge load. *Frontiers of Architecture and Civil Engineering in China*, 5(2), 239–248, 2011.

[24] Chai, J., & Rondonuwu, S. G., Surcharge loading rate for minimizing lateral displacement of PVD improved deposit with vacuum pressure. *Geotextiles and Geomembranes*, 43(6), 558–566, 2015.

[25] Lo, S. R., Mak, J., Gnanendran, C. T., Zhang, R., & Manivannan, G., Long-term performance of a wide embankment on soft clay improved with prefabricated vertical drains. *Canadian Geotechnical Journal*, 45(8), 1073–1091, 2008.

[26] Akan, R., Sert, S., & Bol, E., Killi Zeminler Üzerindeki Yol Dolgularında Konsolidasyonun Hızlandırılması, *In 6th International Symposium on Innovative Technologies in Engineering Science*, 9-11 November. Alanya, Antalya, Turkey, 2018.

[27] Wang, J., Gao, Z., Fu, H., Ding, G., Cai, Y., Geng, X., & Shi, C., Effect of surcharge loading rate and mobilized load ratio on the performance of vacuum–surcharge preloading with PVDs. *Geotextiles and Geomembranes*, 47(2), 121–127, 2019.

[28] Kaisarta, A. M., & Ilyas, T., Finite element modeling of soil improvement using vacuum consolidation with vertical drain method (Case study: Apartment project, Tangerang), *In International Conference on Science, Technology, and Environment*, 59–66, Surabaya, 2020.

[29] Zhafirah, A., Permana, S., Daris, M., & Yogawsara, D., Comparative analysis of soft soil consolidation time due to improvement using prefabricated vertical drain. *IOP Conference Series: Materials Science and Engineering*, 1098(2), 022056, 2021.

[30] Nguyen, T. N., Shukla, S. K., Dang, P. H., Lam, L. G., Khatir, S., & Cuong-Le, T., Numerical modeling of prefabricated vertical drain with vacuum consolidation technique. *Transportation Infrastructure Geotechnology,* 2021.

[31] Nguyen, T., Bergado, D., Kikumoto, M., Dang, P., Chaiyaput, S., & Nguyen, P., A simple solution for prefabricated vertical drain with surcharge preloading combined with vacuum consolidation. *Geotextiles and Geomembranes*, 49, 304–322, 2021.

[32] Syahril, S., The effect of soft clay improvement using prefabricated vertical drain (PVD) for rigid pavement structure. *IOP Conference Series: Materials Science and Engineering*, 1098(2), 022063, 2021.

[33] Tigdemir, M., Jafarzadyeganeh, M., Bayrak, M. Ç., Avcar, M., Numerical modelling of wheel on the snow. *International Journal of Engineering and Applied Sciences*, 10(2), 64–72, 2018.

[34] Bayrak, M. Ç., Avcar, M., Finite element modeling of receding contact problem. *International Journal of Engineering and Applied Sciences*, 11(4), 468–475, 2019.

[35] Mercan, K., Civalek, Ö., Modal analysis of micro and nanowires using finite element softwares. *International Journal Of Engineering & Applied Sciences*, 10(4), 291–304, 2019.

International Journal of Engineering & Applied Sciences (IJEAS)
Vol. 13, Issue 3 (2021) 106-125
http://dx.doi.org/10.24107/ijeas.1019382
Int J Eng Appl Sci 13(3) (2021) 106-125

Application of Artificial Neural Networks to Predict Inhibition in Probiotic Experiments

Ecren Uzun Yaylacı

Karadeniz Technical University, Faculty of Marine Sciences, 61530, Trabzon, Turkey
E-mail address: ecrenuzun@ktu.edu.tr

ORCID numbers of authors:
0000-0002-2558-2487

Received date: 05.11.2021
Accepted date: 06.12.2021

Abstract

Artificial neural networks (ANNs) provide a modeling approach that can be used in the *in vitro* stages of probiotic studies. The aim of the study was to evaluate the ability of multilayer perceptron (MLP) and radial-basis function (RBF) ANNs to predict the inhibition level of indicator bacteria in co-culture experiments performed at various initial concentrations. In both types of networks, time, initial concentrations of *L. lactis* and *Aeromonas* spp. were the input variables and the inhibition concentration of *Aeromonas* spp. was the output value. In the construction of the models, different numbers of neurons in the hidden layer, and different activation functions were examined. The performance of the developed MLP and RBF models was tested with root mean square error (RMSE), coefficient of determination (R^2) and relative error (e) statistical analysis. Both ANN models were showed a strong agreement between the predicted and experimental values. However, the developed MLP models showed higher accuracy and efficiency than the RBF models. The results indicated that ANNs developed in this study can successfully predict the inhibition concentration of *Aeromonas* spp. co-cultured with *L. lactis in vitro* and can be used to determine bacterial concentrations in the design of further experiments.

Keywords: Artificial Neural Network, *In Vitro*, Probiotic

1. Introduction

Aeromonas spp. are Gram-negative opportunistic bacteria with global distribution in various aquatic environments [1-2]. They are divided into two groups as motile and non-motile. The only non-motile *Aeromonas* species is *A. salmonicida* and is one of the important fish pathogens. Motile *Aeromonas* species (MAS) especially *A. hydrophila, A. veronii* and *A. sobria* may infect humans and lower vertebrates, including amphibians, reptiles, and fish [3-4]. MAS are considered as agents of motile aeromonad infections in aquatic animals [5]. MAS infections are characterised with exophthalmia, haemorrhages, ulcerations, skin lesions, acidic fluid, liver and kidney lesions in fish [6]. Motile *Aeromonas* species, especially *A. hydrophila*, cause great economic losses as it initiates outbreaks that cause massive fish mortality worldwide [3]. Antibiotics have been widely used for many years to prevent and control bacterial diseases in aquaculture [7]. The continuous applications of antibiotics cause accumulation of antibiotics in organs, disruption of the normal microbiota of the gut [8], and the development of antibiotic-resistant bacteria [9]. In the last decade, intensive use of antibiotic-based therapies against *Aeromonas* spp. has led to increased resistance of these bacteria to antibiotics such as oxytetracycline, tetracycline, and trimethoprim/sulfamethoxazole [10]. Therefore,

© 2021 E.U. Yaylacı published by International Journal of Engineering & Applied Sciences. This work is licensed under a Creative Commons Attribution-NonCommercial-ShareAlike 4.0 International License

environmentally friendly biocontrol agents such as probiotics can be used as an alternative approach to reduce these risk factors [11-12].

The use of probiotics is considered as an alternative method to prevent bacterial infections in aquaculture [13-14]. Lactic acid bacteria (LAB) are widely preferred in aquaculture as they are effective in disease control, improve intestinal microbial balance [15] and promote growth by increasing immune response [16]. LAB are "generally recognized as safe" (GRAS) microorganisms [17] and they are permanent inhabitants of the fish intestinal flora [18]. LAB produce various antimicrobial compounds such as organic acid, ethanol, hydrogen peroxide, diacetyl, carbon dioxide and bacteriocin that inhibit the growth of pathogenic bacteria [19-21]. The use of bacteriocins against *Aeromonas* spp. is an alternative method of inhibiting their growth [22]. Bacteriocins such as bacteriocin ST151BR, bacteriocin HKT-9 and plantarisin 35d secreted by LAB are effective against *Aeromonas* spp. has been previously reported in several papers [23-24].

There are many well-defined and commercially used probiotic strains worldwide, but the discovery of new strains still arouses the interest of scientists [25]. Many *in vitro* and *in vivo* methods are used in probiotic experiments. *In vivo* testing is expensive, time-consuming, and requires ethical committee approval. Therefore, reliable *in vitro* methods are required for the selection of potential probiotic strains [26]. *In vitro* tests are quite different from *in vivo* conditions, but they provide rapid and efficient screening for the search for new potential LAB strains [27-28]. Determination of bacterial growth or inactivation kinetics under ideal laboratory conditions are the methods applied in probiotic studies. Besides that, the mathematical modelling is preferred as a suitable tool for selecting beneficial strains, designing laboratory equipments, and determining growth parameters [29]. Predictive microbiology focuses on mathematical models that describe the effect of factors such as temperature, pH, concentration, and inactivation kinetics of microbial growth [30]. In statistical models, it is difficult to express relationships between categorical data such as bacterial names, bacterial behavior and environmental parameters. Because categorical data are qualitative values and arithmetic operations cannot be performed [31]. Therefore, an alternative approach is required that can process large noisy datasets, learn relationships directly from the result of experiments, and predict without prior knowledge. In recent years, artificial neural networks (ANNs), which can describe nonlinear and complex relationships between data without any assumptions, have become an alternative to traditional regression models [32-33]. These are used to predict the outcome of any problem or situation in different disciplines by using some input values and relations [34]. ANNs imitate the functioning of the human brain. They can learn, recognize, and overcome complex problems in engineering and science [35]. A general ANN system consists of layers. The input layer receives signals from the external environment. There is no transaction in this layer. The hidden layer processes the information from the input layer. It can contain more than one layer. The output layer takes the weighted sum of the outputs of all hidden layer neurons and produces the output of the model [36].

The aim of this work was to examine the ability of ANNs to predict the inhibition concentration of *Aeromonas* spp. co-cultured with *Lactococcus lactis*. Two computational models based on the ANN approach are presented for the prediction. These models are, multilayer perceptron (MLP) and radial basis function (RBF). The data set was obtained from co-culture experiments performed in a controlled laboratory condition. The accuracy and validity of the developed MLP and RBF models were compared with the actual experimental results.

2. Materials and Methods

2.1. Microorganisms and experimental design

Microorganisms used in this study included *Lactococcus lactis* (MG754705.1), *Aeromonas veronii* (MG322191.1), *Aeromonas sobria* (ATCC 43979) and *Aeromonas hydrophila* (ATCC 7966). *L. lactis* and *A. veronii* were isolated from fish (*Dicentrarchus labrax*) and confirmed by sequencing of their 16S rRNA gene [37]. *L. lactis* was selected for its probiotic properties and *Aeromonas* species were used as indicator strains. Live *L. lactis* cells were selected because the inhibitory effect was better than the supernatants (unpublished data).

Experiments were carried out at different initial concentrations. These are 1.0×10^4 cfu /mL, 1.0×10^6 cfu /mL and 1.0×10^8 cfu /mL for indicator bacteria and 1.0×10^4 cfu/mL, 1.0×10^5 cfu/mL, 1.0×10^6 cfu /mL, 1.0×10^7 cfu/mL and 1.0×10^8 cfu/mL for *L. lactis*. *L. lactis* was co-cultured with each of the indicator bacteria separately at the indicated initial concentrations in tryptic soy broth (TSB) at 30 °C, pH 7.2 for 120 h (150 rpm^{-1} in a shaker). Uncultivated TSB was used as a negative control. Samples (100 µl) withdrawn 0, 6, 24, 30, 48, 54, 72, 78, 96, 102 and 120 h from the fermented cultures and colonies were counted using the standard agar plate method. deMan Rogosa Sharpe (MRS) agar plates were used to select *Lactococcus*, while thiosulfate citrate bile salts sucrose agar (TCBS) plates were used for *Aeromonas*. The number of bacteria from plate counts were calculated as log values, which is a transformation of the microbiological data stabilizing the variance [38-39].

2.2. Data sets used for modeling

The input values in the networks represent the initial concentrations of *L. lactis*, *Aeromonas* spp. and the sampling times during fermentation. The estimated value of the developed networks is the concentration of *Aeromonas* spp. (cfu/mL) at the selected sampling points. The database consisted of 495 experimental data. These experimental data were divided into two groups as training and validation data sets. The models were built with training data (270 data, 3 indicator strains × 90 sampling points per strain) which are different combinations of the values in Table 1. The remaining data (225 data, 3 indicator strains × 75 sampling points per strain) obtained at 6, 30, 54, 78, and 102 h was not added to the training data set, it was used for the model validation. These sampling points were selected to cover the entire co-culture process [39].

Table 1. Test parameters

Time (h)	*L. lactis* (cfu/mL)*	*Aeromonas* spp. (cfu /mL)*
0	1.0×10^8	1.0×10^8
24	1.0×10^7	1.0×10^6
48	1.0×10^6	1.0×10^4
72	1.0×10^5	
96	1.0×10^4	
120		

* initial concentrations

2.3. Development of MLP and RBF models

Multilayer perceptron and radial basis function are the most preferred algorithms of neural networks and are used to solve many problems. These algorithms belong to a general class of neural networks called feed-forward neural networks. In this network type, the information processing follows one direction from input neurons to output neurons [40]. In MLP and RBF, each neuron is independent in its layer but is connected to all neurons in the next layer with certain weights [41]. While there is no transaction in the input layer, the hidden layer and output layers process the data using the activation function. There are some differences between MLP and RBF neural networks [42]. The first and the most important difference between MLP and RBF networks is that they generate different learning strategies against problems [39]. RBFs generate local solutions and network outputs are obtained by specified hidden neurons in certain local accessible areas, while MLPs act globally, and network outputs are decided by all neurons [42, 43]. In MLP networks, input signal activates many neurons, and these activated neurons participate in the calculation of the network output. In RBF networks, input signal activates a single neuron of the hidden layer and the weight between the activated hidden and output neurons participates in the calculation of the network output [44]. Second, MLP networks are structured one or several hidden layers, while RBF networks always have single hidden layer. Third, in MLP networks, neurons of the hidden layer usually contain a sigmoidal activation function (i.e., a logistic or hyperbolic tangent function), while in RBF networks, a radial-based activation function (usually a gaussian function).

The input and output values of each pattern were normalized in the range of 0.1–0.9. The number of neurons in the hidden layer ranged from 2-20 for MLP networks and 2-30 for RBF networks. Weights are initialized into random values between 0.0001 and 0.001. The appropriateness values of the error functions (sum of squares and entropy) were tested. After the network type is determined, the activation functions that transfer the signals from the previous layer to the next layer using a mathematical function are selected. In MLP networks, identity, logistic sigmoid, hyperbolic tangent, exponential, softmax, and gaussian activation functions were examined, and in RBP networks gaussian was tested. The architecture of MLP and RBF neural networks are illustrated in Fig 1. In this study, BFGS (Broyden-Fletcher-Goldfarb-Shanno) for MLP networks and RBFT (Reputation-based Byzantine Fault Tolerance) training algorithms for RBF networks were examined. 5000 networks were developed for MLP structures and 10000 networks for RBF-based structures. An artificial neural network model was performed in Statistica software 12 using the neural network module. The program code was written in C++ language.

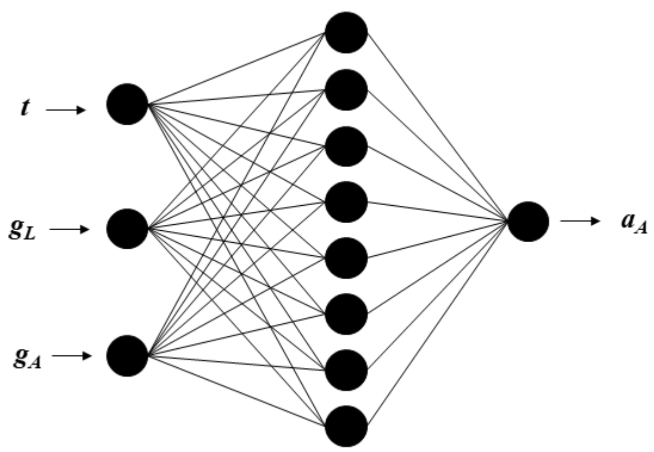

Fig. 1. The architecture of MLP and RBF neural networks

2.4. Model performance

In the study, the performance and accuracy of proposed MLP and RBF neural network models were tested with statistical parameters. The coefficient of determination (R^2), root mean square error (RMSE) and relative error (e) were used to conclude about the accuracy of both neural network models. These parameters calculated as follows:

$$RMSE = \sqrt{\frac{1}{n}\sum_{i}^{n}\left(R_{\exp_i} - R_{ANN_i}\right)^2}, \qquad (i = 1,2,3,...,n) \tag{1}$$

$$R^2 = 1 - \frac{\sum_{i}^{n}\left(R_{\exp_i} - R_{ANN_i}\right)^2}{\sum_{i}^{n}\left(R_{\exp_i} - \overline{R}_{\exp}\right)^2}, \qquad (i = 1,2,3,...,n) \tag{2}$$

$$e = \left|\frac{R_{\exp_i} - R_{ANN_i}}{R_{\exp_i}}\right| \text{x}100, \qquad (i = 1,2,3,...,n) \tag{3}$$

Where R_{expi} and E_{ANNi} are the experimental and calculated (with MLP and RBF) concentrations of the *A. veronii, A. hydrophila* and *A. sobria. n* denotes the total number of sampling points and $\bar{R}_{exp}$ refers to average experimental value.

3. Result and Discussion

Co-culture experiments are the preferred method for evaluating the inhibition activity of *L. lactis* [45]. In this study, co-culture experiments of *L. lactis* with *A. veronii, A. hydrophila* and *A. sobria* were performed. The highest inhibition rate was detected after 120 h of incubation with *Aeromonas* spp. with an initial level of 1.0 × 10^4 cfu/mL and *L. lactis* with an initial level of 1.0 × 10^8 cfu/mL. The inhibition rates were determined 54.4% for *A. veronii,* 48.3% for *A. hydrophila* and 38.8% for *A. sobria.* In agreement with previous studies, co-culture experiments showed that the inhibitory activity of *L. lactis* increased when the concentration of probiotic bacteria and the incubation time increased [46].

Gathering sufficient and valid data is one of the most important steps in the mathematical model development process [40]. In this study, a total of 495 experimental data obtained from *in vitro* co-culture assays of *A. veronii, A. sobria, A. hydrophila* with *L.lactis* were used in order to develop MLP and RBF models. 270 of these data were used to build the model while 225 of them were used to validation. Each set of data includes sampling points during co-culture assay and amounts of *L. lactis* and *Aeromonas* spp.

In this study, the comparison of the empirical correlations of the proposed models was evaluated by considering the root mean square error (RMSE), coefficient of determination (R^2) and relative error (e) statistical parameters. A lower RMSE value exhibits better efficiency [40]. The fact that the RMSE value is close to zero indicates that the predictive ability of the model has increased [47]. Although the RMSE values of the two networks are close to each other, the RMSE values of MLP are lower than RBF models. R^2 is a statistical definition that reveals the numerical relationship between the data obtained from the experiment results and the network model predictions [43]. This value is defined as the square of the correlation coefficient and ranges from 0 to 1. $R^2 > 0.80$ means that there is a strong correlation between experimental values and model predictions [48]. R^2 values of MLP were slightly higher than RBF models. A relative error is a type of error that shows how close the obtained values are to the real values. It was determined that MLP models had lower relative error rates than RBF models. Figures 2, 4 and 6 indicate that both models exhibited high correlation coefficients. The high accuracy of the proposed models shows that these models have been successfully trained [40]. Although there are small differences between the RMSE, R^2 and relative error values of both methods, it is seen that the MLP model has a better estimation capacity than the RBF model.

Figures 3, 5 and 7 show a comparison of the experimental results with the predictions of the MLP and RBF models as a function of time. It was determined that there is a high match between MLP models and experimental results. In the RBF models, it was determined that the predictions converged less with the data of the experimental results.

The RMSE of *A. veronii* was calculated as $RMSE_{MLP}=0.072111$ and $RMSE_{RBF}=0.084063$. The R^2 of *A. veronii* was calculated as $R^2_{MLP}=0.998224$ and $R^2_{RBF}=0.997195$ (Fig. 2).

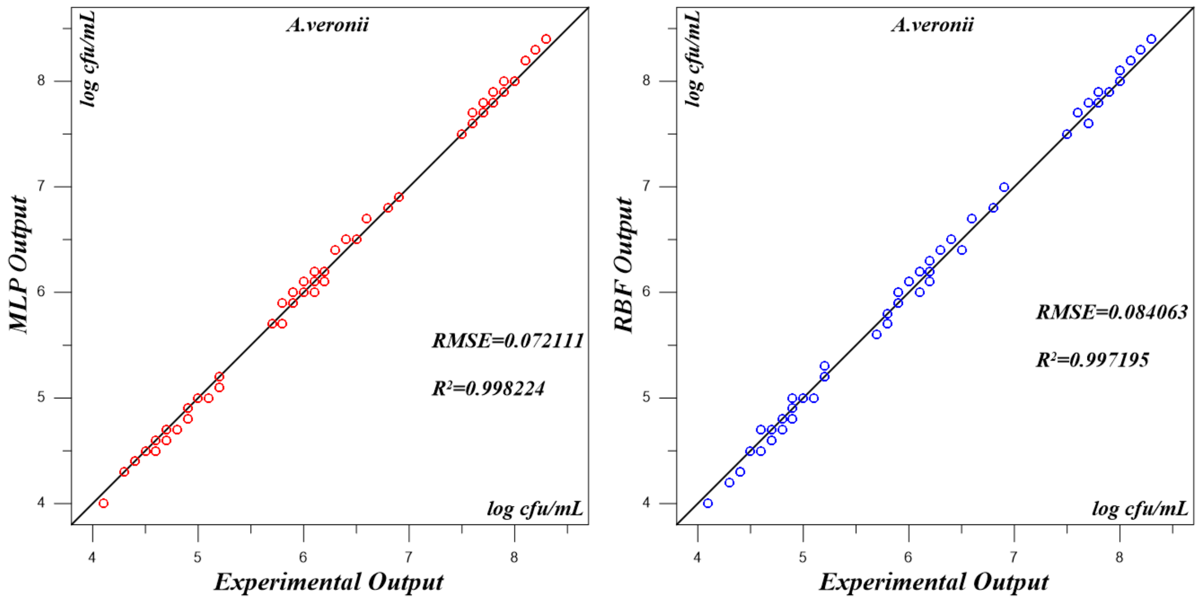

(a) (b)

Fig. 2. Correlation between neural network model predictions and experimental outputs for *A. veronii*

Figure 3 shows the amount of *A. veronii* co-cultured with *L. lactis*. As shown in the figure, the average relative errors of *A. veronii* were calculated as $e_{MLP}=0.85\%$ and $e_{RBF}=1.19\%$.

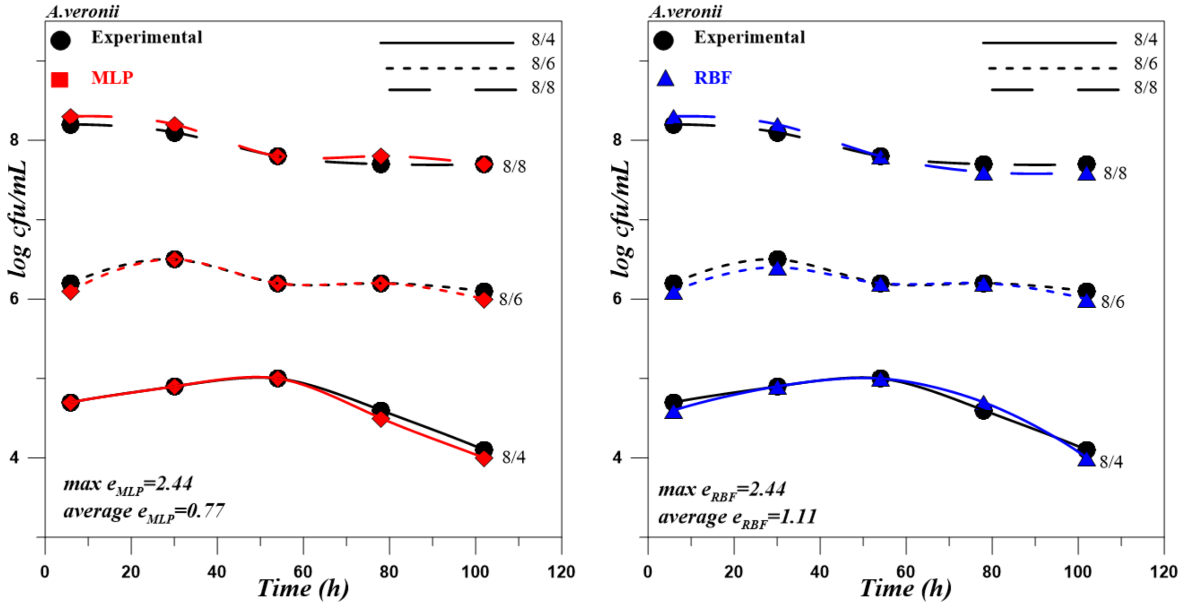
A.veronii
Experimental
MLP
8/4
8/6
8/8
log cfu/mL
Time (h)
max e_MLP=2.44
average e_MLP=0.77
A.veronii
Experimental
RBF
8/4
8/6
8/8
log cfu/mL
Time (h)
max e_RBF=2.44
average e_RBF=1.11

(a)

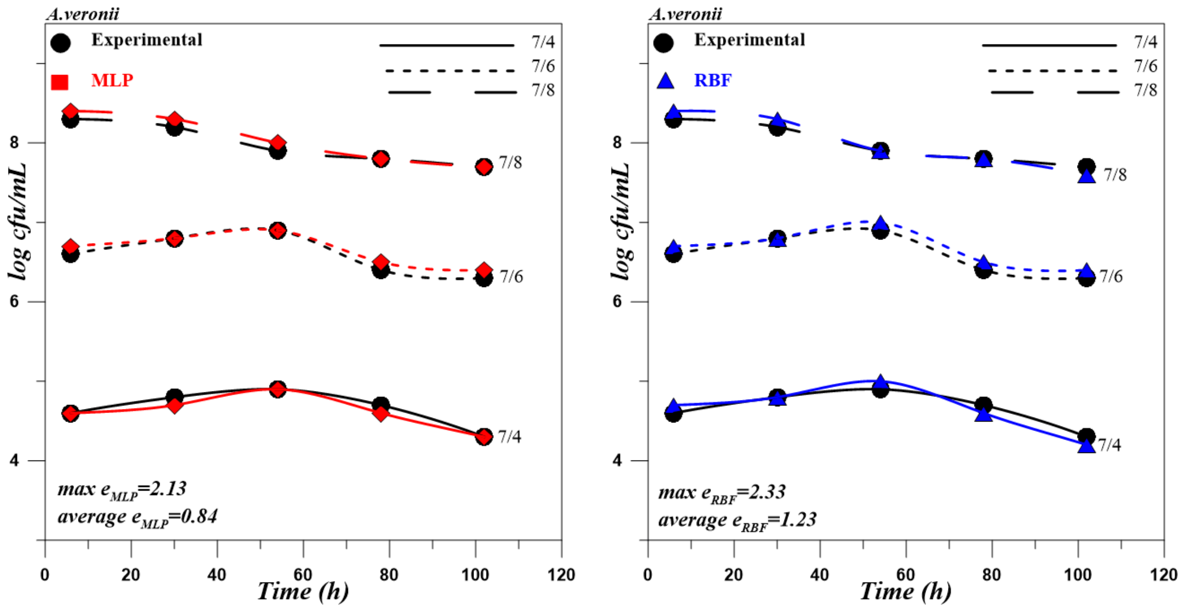
A.veronii
Experimental
MLP
7/4
7/6
7/8
log cfu/mL
Time (h)
max e_MLP=2.13
average e_MLP=0.84
A.veronii
Experimental
RBF
7/4
7/6
7/8
log cfu/mL
Time (h)
max e_RBF=2.33
average e_RBF=1.23

(b)

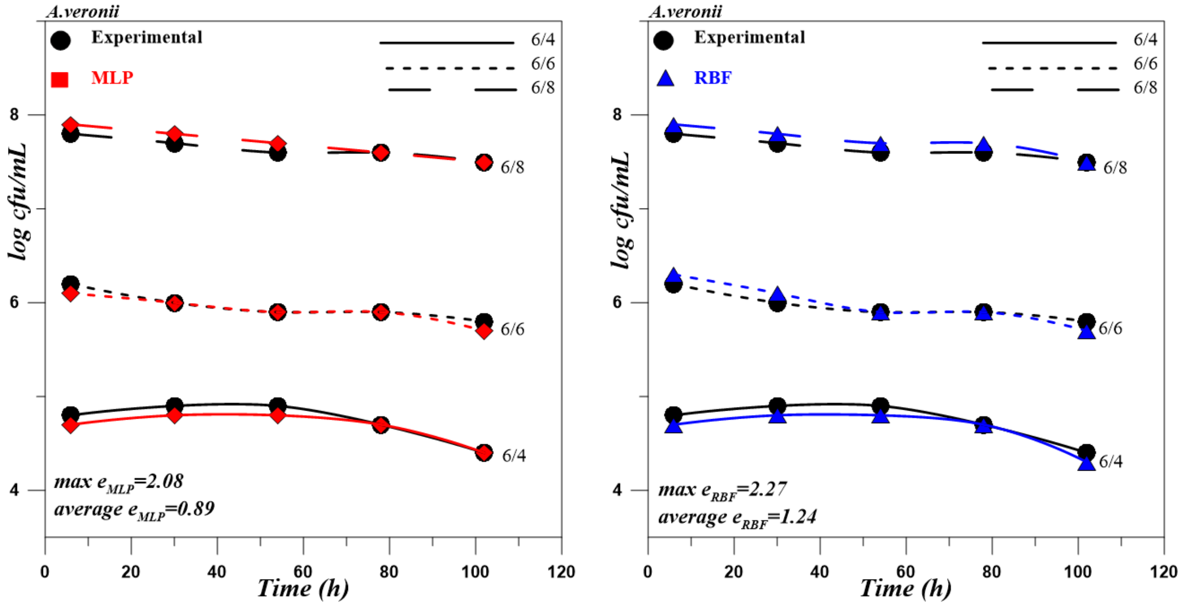
A.veronii
Experimental
MLP
6/4
6/6
6/8
max e_{MLP}=2.08
average e_{MLP}=0.89
log cfu/mL
Time (h)
A.veronii
Experimental
RBF
6/4
6/6
6/8
max e_{RBF}=2.27
average e_{RBF}=1.24
log cfu/mL
Time (h)

(c)

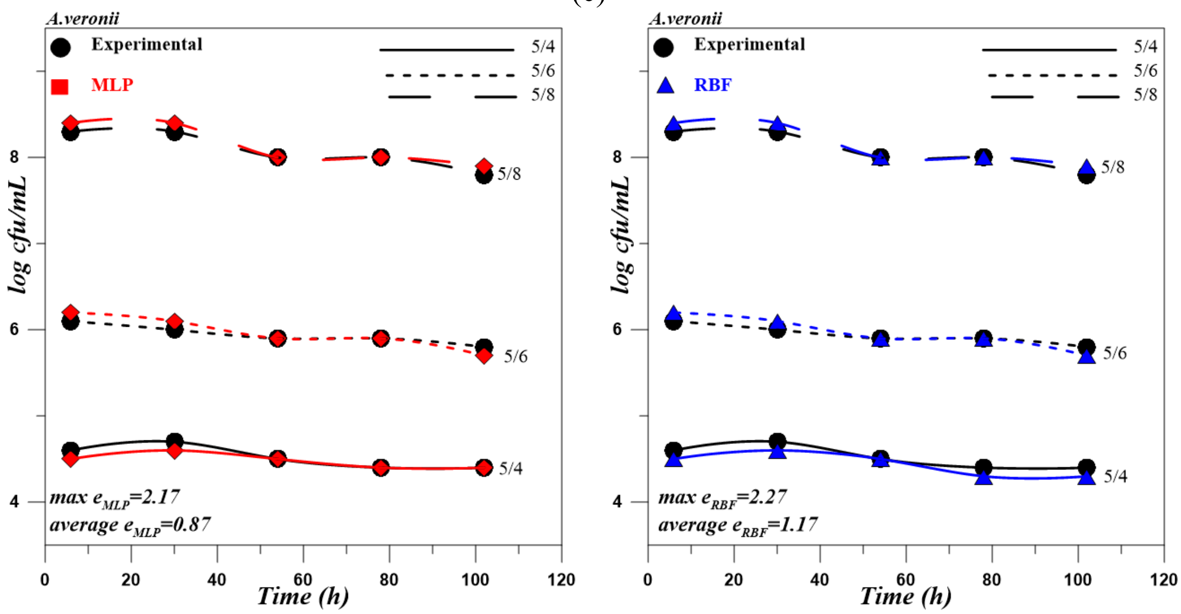
A.veronii
Experimental
MLP
5/4
5/6
5/8
max e_{MLP}=2.17
average e_{MLP}=0.87
log cfu/mL
Time (h)
A.veronii
Experimental
RBF
5/4
5/6
5/8
max e_{RBF}=2.27
average e_{RBF}=1.17
log cfu/mL
Time (h)

(d)

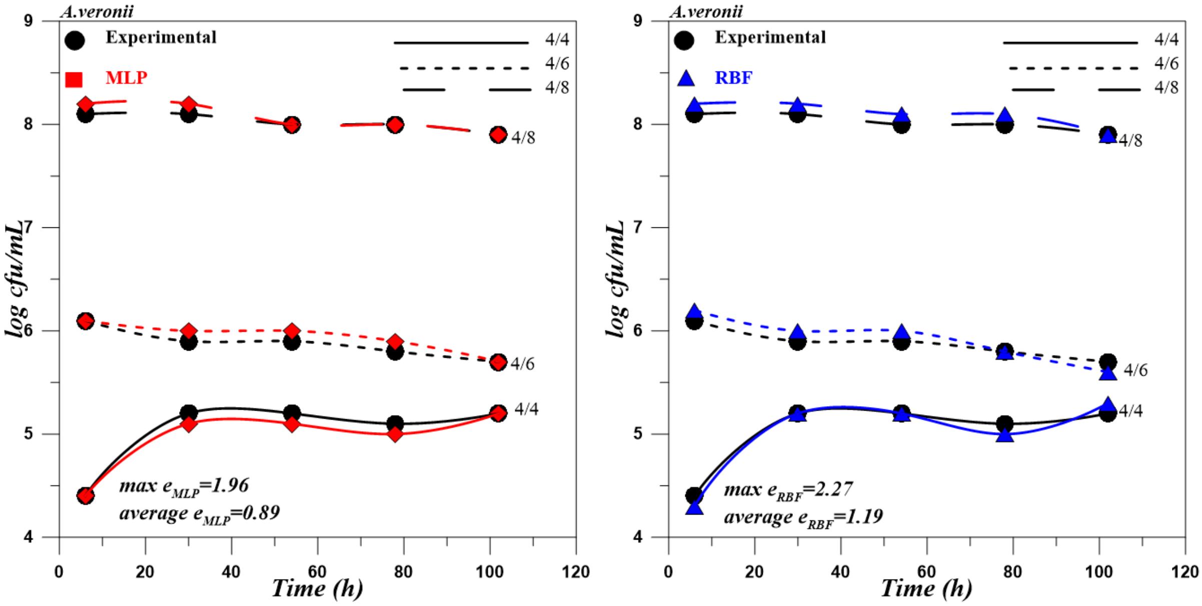

(e)

Fig. 3. The comparison of neural network model predictions and experimental outputs for the concentrations of *A. veronii* co-cultured with *L. lactis*. The initial concentrations of *A. veronii* were 1.0×10^4 cfu/mL, 1.0×10^6 cfu/mL and 1.0×10^8 cfu/mL and initial concentrations of *L. lactis* were (a) 1.0×10^8 cfu/mL (b) 1.0×10^7 cfu/mL (c) 1.0×10^6 cfu/mL (d) 1.0×10^5 cfu/mL (e) 1.0×10^4 cfu/mL

The RMSE of *A. hydrophila* was calculated as $RMSE_{MLP}$=*0.073937* and $RMSE_{RBF}$ =*0.084853*. The R^2 of *A. hydrophila* was calculated as R^2_{MLP}=*0.996797* and R^2_{RBF}=*0.995645* (Fig. 4).

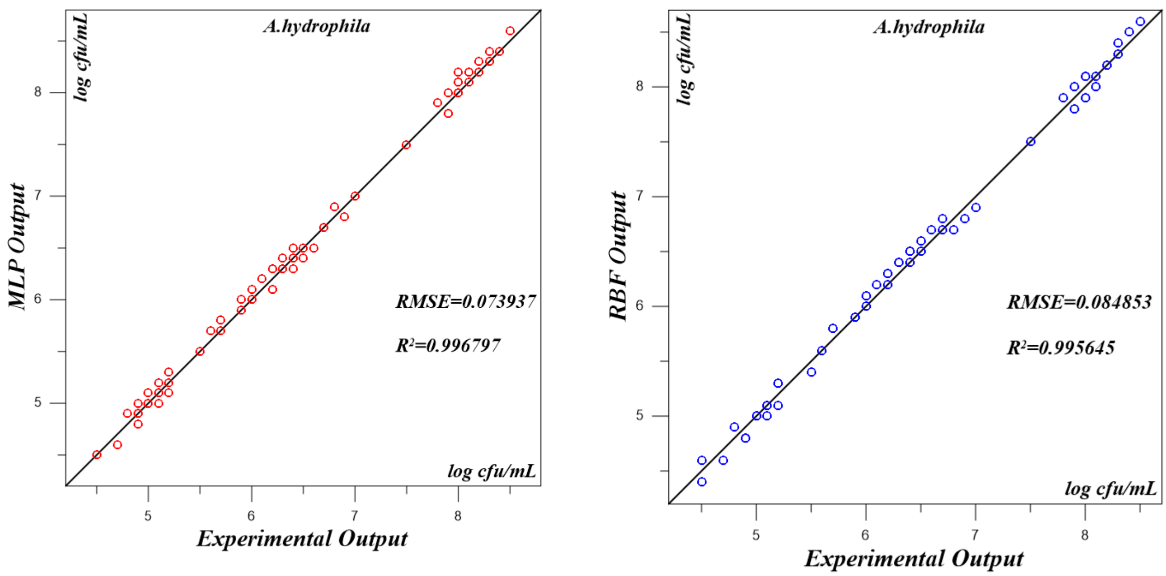

(a) (b)

Fig. 4. Correlation between neural network model predictions and experimental outputs for *A. hydrophila*

Figure 5 shows the concentrations of *A. hydrophila* co-cultured with *L. lactis*. As shown in the figure, the average relative errors of *A. hydrophila* were calculated as $e_{MLP}=0.82\%$ and $e_{RBF}=1.15\%$.

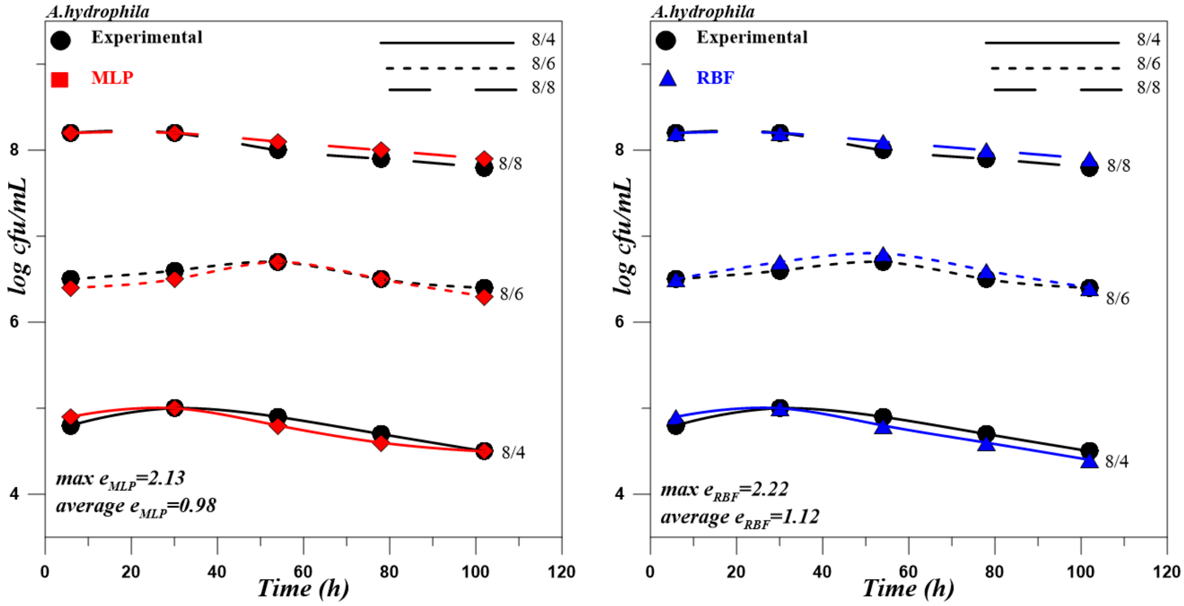

(a)

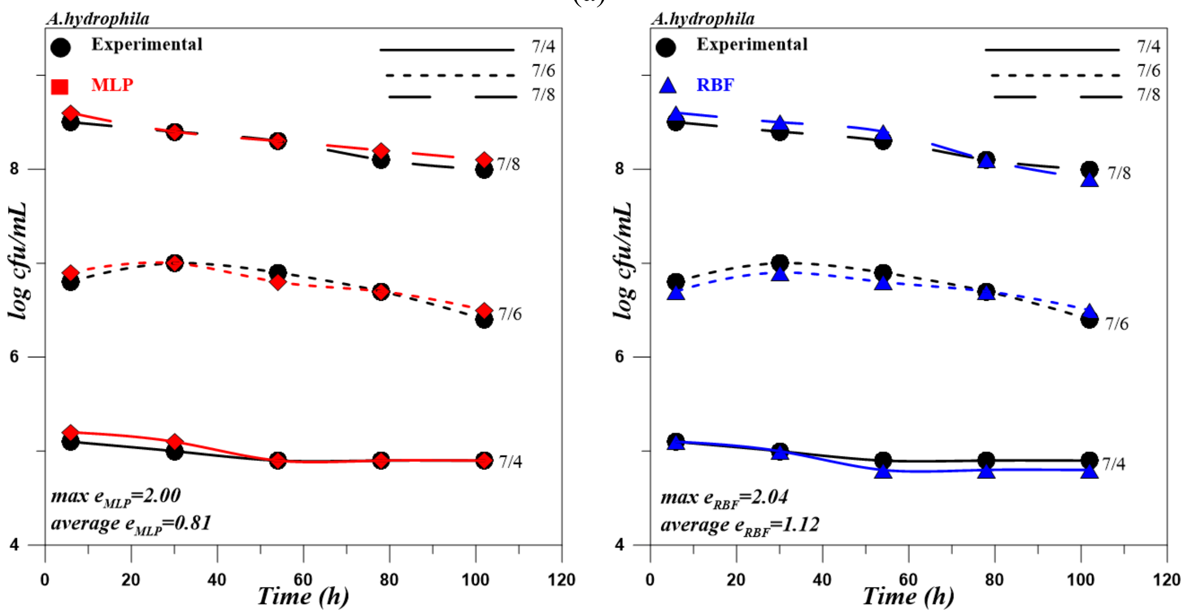

(b)

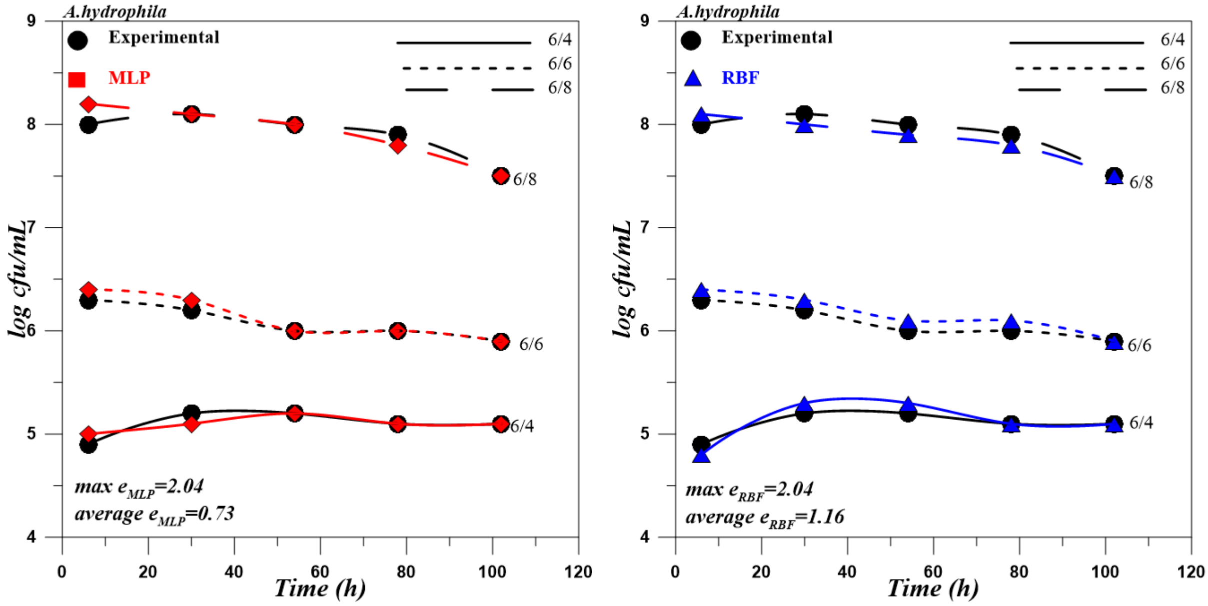
A.hydrophila
Experimental
MLP
6/4
6/6
6/8
max e_{MLP}=2.04
average e_{MLP}=0.73
log cfu/mL
Time (h)
A.hydrophila
Experimental
RBF
6/4
6/6
6/8
max e_{RBF}=2.04
average e_{RBF}=1.16
log cfu/mL
Time (h)

(c)

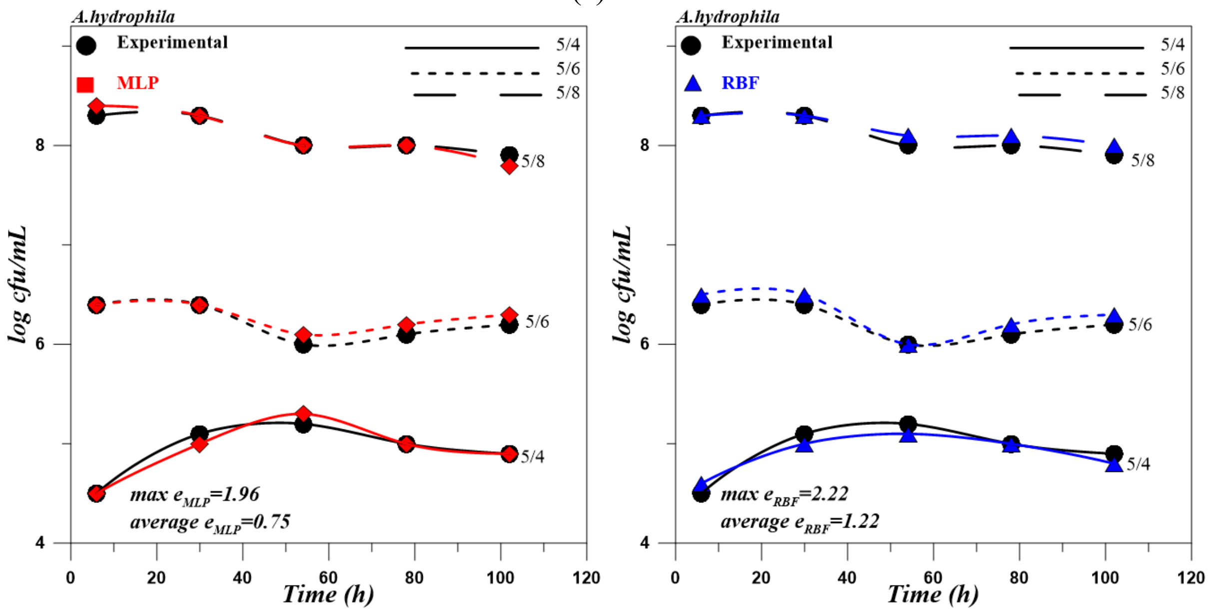
A.hydrophila
Experimental
MLP
5/4
5/6
5/8
max e_{MLP}=1.96
average e_{MLP}=0.75
log cfu/mL
Time (h)
A.hydrophila
Experimental
RBF
5/4
5/6
5/8
max e_{RBF}=2.22
average e_{RBF}=1.22
log cfu/mL
Time (h)

(d)

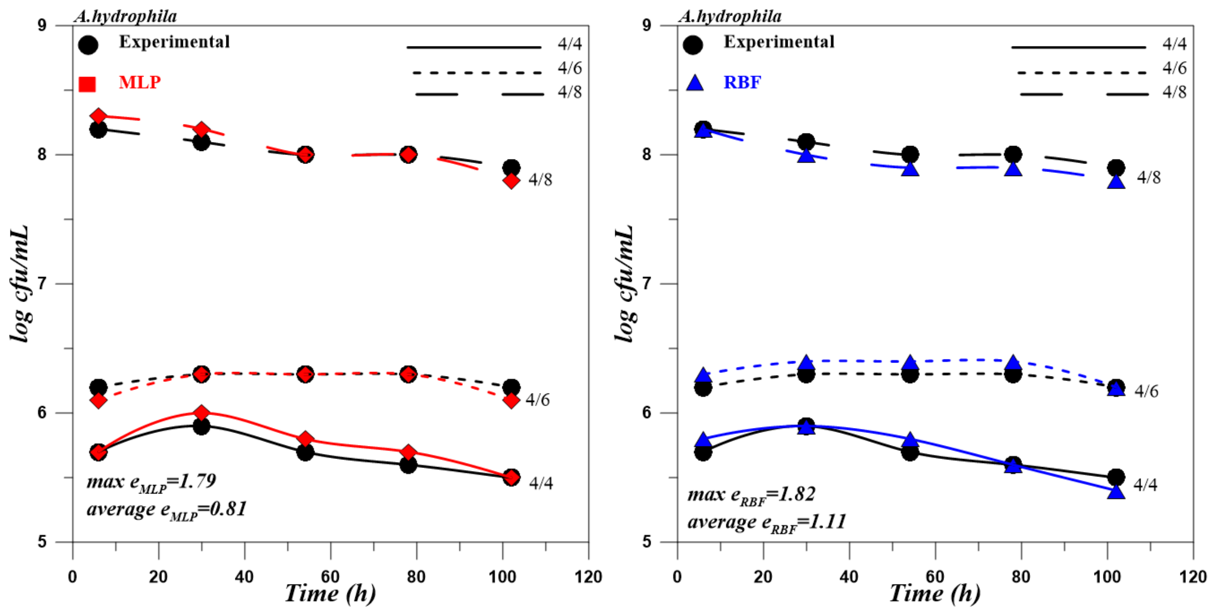

(e)

Fig. 5. The comparison of neural network model predictions and experimental outputs for the concentrations of *A. hydrophila* co-cultured with *L. lactis*. The initial concentrations of *A. hydrophila* were 1.0×10^4 cfu/mL, 1.0×10^6 cfu/mL and 1.0×10^8 cfu/mL and initial concentrations of *L. lactis* were (a) 1.0×10^8 cfu/mL (b) 1.0×10^7 cfu/mL (c) 1.0×10^6 cfu/mL (d) 1.0×10^5 cfu/mL (e) 1.0×10^4 cfu/mL

The RMSE of *A. sobria* was calculated as $RMSE_{MLP}$=*0.071181* and $RMSE_{RBF}$=*0.084063*. The R^2 of *A. sobria* was calculated as R^2_{MLP}=*0.996865* and R^2_{RBF}=*0.995571* (Fig. 6).

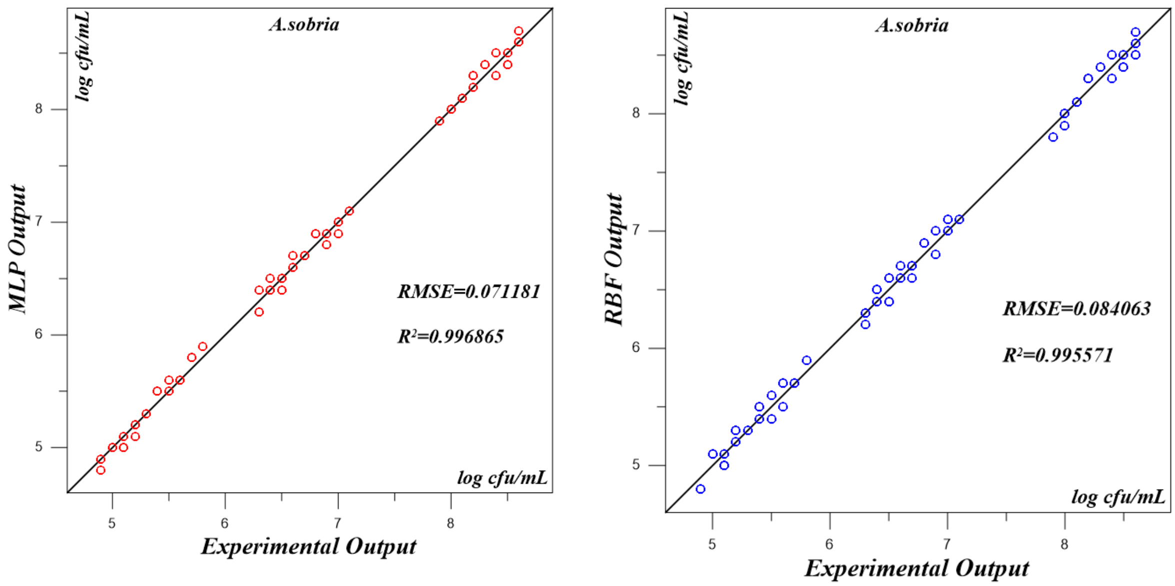

Fig. 6. Correlation between neural network model predictions and experimental outputs for *A.sobria*

Figure 7 shows the concentrations of *A. sobria* co-cultured with *L. lactis*. As shown in the figure, the average relative errors of *A. sobria* were calculated as e_{MLP}=*0.79%* and e_{RBF}=*1.10%*.

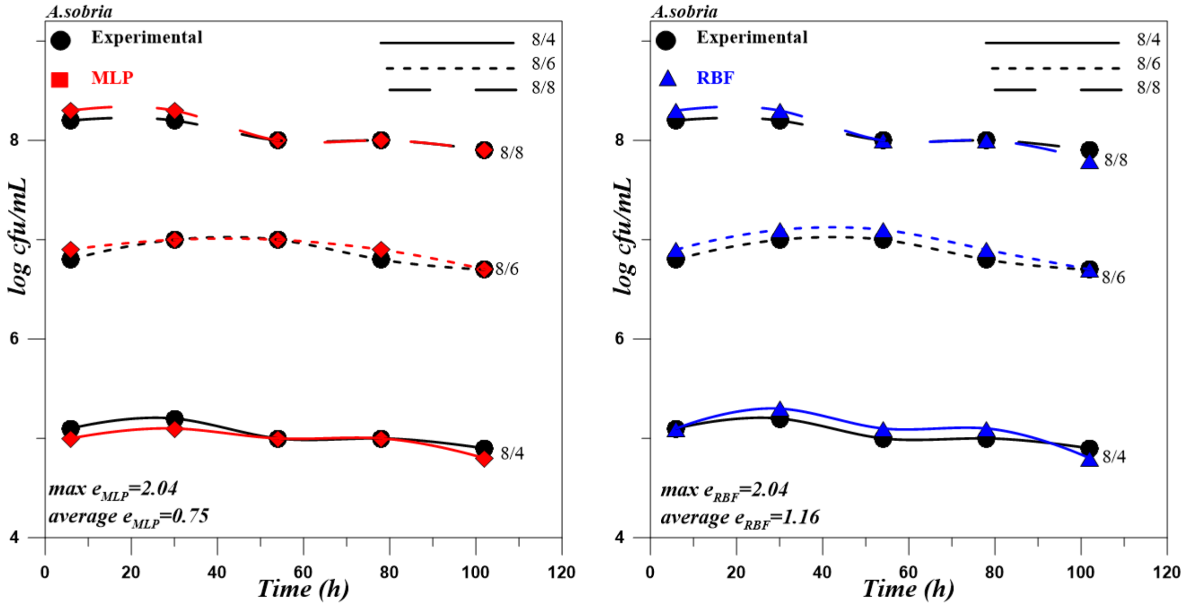
A.sobria
Experimental
MLP
8/4
8/6
8/8
log cfu/mL
max e_{MLP}=2.04
average e_{MLP}=0.75
Time (h)
A.sobria
Experimental
RBF
8/4
8/6
8/8
log cfu/mL
max e_{RBF}=2.04
average e_{RBF}=1.16
Time (h)

(a)

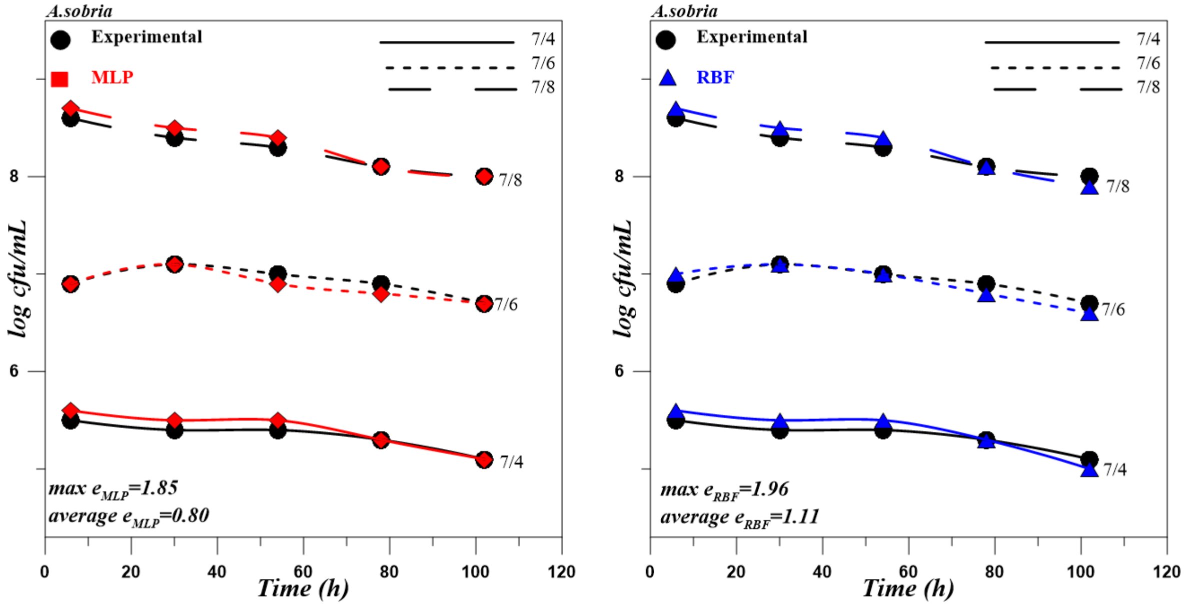
A.sobria
Experimental
MLP
7/4
7/6
7/8
log cfu/mL
max e_{MLP}=1.85
average e_{MLP}=0.80
Time (h)
A.sobria
Experimental
RBF
7/4
7/6
7/8
log cfu/mL
max e_{RBF}=1.96
average e_{RBF}=1.11
Time (h)

(b)

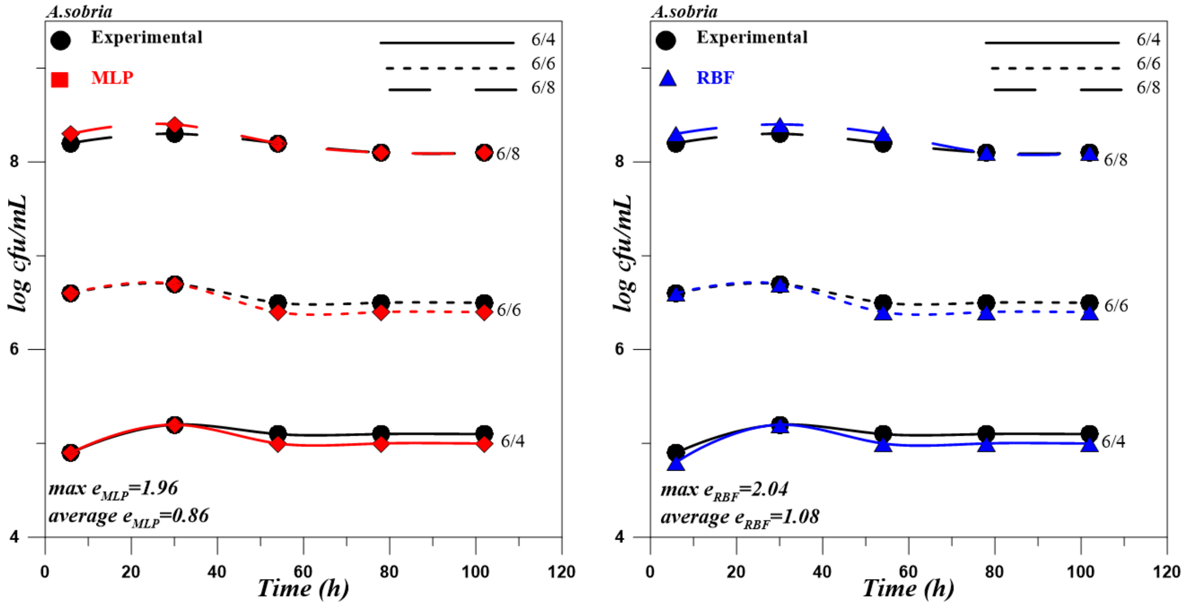
A.sobria
Experimental
MLP
6/4
6/6
6/8
max e_{MLP}=1.96
average e_{MLP}=0.86
log cfu/mL
Time (h)
A.sobria
Experimental
RBF
6/4
6/6
6/8
max e_{RBF}=2.04
average e_{RBF}=1.08
log cfu/mL
Time (h)

(c)

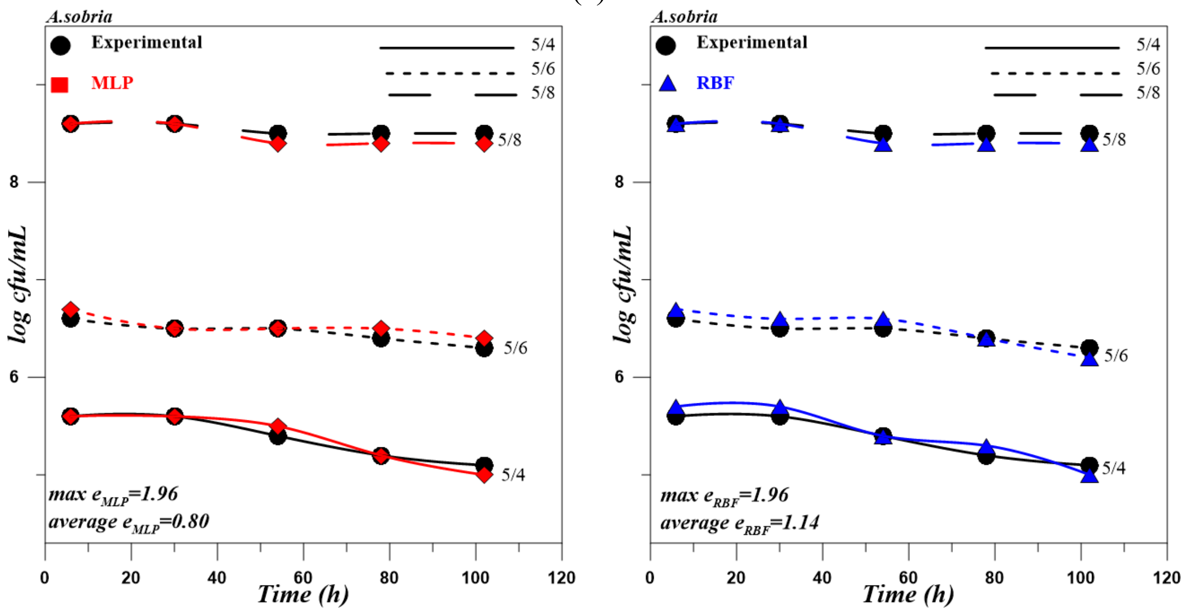
A.sobria
Experimental
MLP
5/4
5/6
5/8
max e_{MLP}=1.96
average e_{MLP}=0.80
log cfu/mL
Time (h)
A.sobria
Experimental
RBF
5/4
5/6
5/8
max e_{RBF}=1.96
average e_{RBF}=1.14
log cfu/mL
Time (h)

(d)

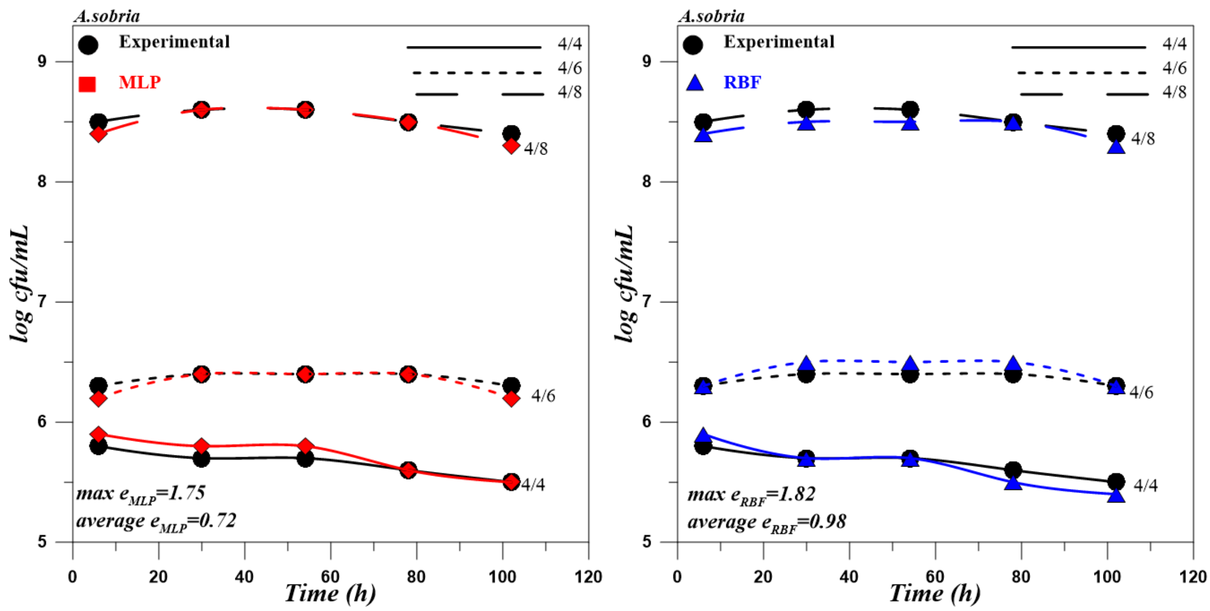

(e)

Fig. 7. The comparison of neural network model predictions and experimental outputs for the concentrations of *A. sobria* co-cultured with *L. lactis*. The initial concentrations of *A. sobria* were 1.0 × 10^4 cfu/mL, 1.0 × 10^6 cfu/mL and 1.0 × 10^8 cfu/mL and initial concentrations of *L. lactis* were (a) 1.0 × 10^8 cfu/mL (b) 1.0 × 10^7 cfu/mL (c) 1.0 × 10^6 cfu/mL (d) 1.0 × 10^5 cfu/mL (e) 1.0 × 10^4 cfu/mL

The optimization processes were performed on different parameters of MLP and RBF models to determine the network architecture with the highest accuracy and efficiency in estimating the concentration of *Aeromonas* spp. in co-culture with *L. lactis*. The number of neurons in the input and output layers can be determined according to the requirements in the problem, but there is no rule in determining the number of process elements in the hidden layers. A network model with an insufficient or excessive number of neurons in the hidden layer can cause poor generalization and overfitting [49]. The best generalization performance is achieved by trial and error versus network complexity [50]. In the current study, the best MLP and RBF network structures were determined by testing multiple architectures and considering the error rates of the networks. In MLP models the most appropriate network configuration was 3 units for each hidden layer with logistic activation function in hidden and output layer. The number of neurons in the hidden layer was different in the RBF models, but in all models the activation function was gaussian in the hidden layer and identity in the output layer. Both network types, with the error term sum of squares (sos) produced superior networks. The best of the neural networks recognized are shown in Table 2.

Table 2. Characteristics of artificial networks that recognize output elements

Network	ANN network model	Learning error	Testing error	Validation error	Learning algorithm	Error function	Activation function in hidden layer	Activation function in output layer
N_1	MLP 3-14-1	0.96	0.73	5.44	BFGS 105	SOS	Logistic	Logistic
	RBF 3-28-1	1.26	1.26	2.11	RBFT	SOS	Gaussian	Identity
N_2	MLP 3-3-1	2.31	4.13	2.13	BFGS 0	SOS	Exponential	Logistic
	RBF 3-26-1	1.0	6.21	2.49	RBFT	SOS	Gaussian	Identity
N_3	MLP 3-3-1	0.85	0.76	0.88	BFGS 37	SOS	Logistic	Logistic
	RBF 3-27-1	0.41	1.83	1.85	RBFT	SOS	Gaussian	Identity

N_1 *A. veronii* network, N_2 *A. hydophila* network, N_3 *A. sobria* network, BFGS Broyden Fletcher Goldfarb-Shanno, RBFT Reputation-based Byzantine Fault Tolerance, SOS sum of squares

4. Conclusion

In this study, two different ANN algorithms, multilayer perceptron (MLP) and radial basis function (RBF) were developed for the prediction of the concentrations of *Aeromonas* spp. co-cultured with *L.lactis*. The performance and accuracy of proposed MLP and RBF models were tested with the coefficient of determination (R^2), root mean square error (RMSE) and relative error (e). Both ANN models were showed a strong agreement between the predicted and experimental values. However, the developed MLP models showed higher accuracy and efficiency compared to the RBF models. The results showed that MLP-based models were successful in estimating the concentrations of *Aeromonas* spp. co-cultured with *L. lactis in vitro* at different initial concentrations over time. Therefore, this model can be used to determine the bacterial concentrations in the designing of further experiments. Since the network was developed from experimental results under controlled laboratory conditions with environmental parameters kept constant, further research should be conducted to test the applicability of the ANN approach in the variability of these parameters.

References

[1] Burke, V., Robinson, J., Cooper, M., Beaman, J., Partridge, K., Peterson, D. and Gracey, M., Biotyping and virulence factors in clinical and environmental isolates of *Aeromonas* species, *Applied and Environmental Microbiology*, 47, 1146–1149, 1984.

[2] Monfort, P. and Baleux, B., Dynamics of *Aeromonas hydrophila, Aeromonas sobria*, and *Aeromonas caviae* in a sewage treatment pond, *Applied and Environmental Microbiology,* 56, 1999–2006, 1990.

[3] Janda, J.M. and Abbott, S.L., Evolving concepts regarding the genus *Aeromonas*: an expanding Panorama of species, disease presentations, and unanswered questions. *Clinical Infectious Diseases,* 27:332–344.1998.

[4] Teunis, P. and Figueras, M.J., Reassessment of the Enteropathogenicity of mesophilic *Aeromonas* Species, *Frontiers in Microbiology,* 7, 1395, 2016.

[5] John, N. and Hatha, A.A.M., Distribution, extracellular virulence factors and drug resistance of motile aeromonads in freshwater ornamental fishes and associated carriage water. *International Journal of Fisheries and Aquaculture,* 3, 92–100, 2013.

[6] Garcia, F., Pilarski, F., Onaka, E.M, de Moraes, F.R. and Martins, M.L., Hematology of *Piaractus mesopotamicus* fed diets supplemented with vitamins C and E, challenged by *Aeromonas hydrophila*. *Aquaculture,* 271, 39–46, 2007.

[7] Done, H.Y., Venkatesan, A.K. and Halden, R.U., Does the recent growth of aquaculture create antibiotic resistance threats different from those associated with land animal production in agriculture? *The AAPS Journal,* 17, 513–524. 2015.

[8] Khemariya, P., Singh, S., Nath, G. and Gulati, A.K., Probiotic *Lactococcus lactis*: A review. *Turkish Journal of Agriculture - Food Science and Technology*, 556–652, 2017.

[9] Resende, J.A., Silva, V.L., Fontes, C.O., et al., Multidrug-resistance and toxic metal tolerance of medically important bacteria isolated from an aquaculture system, *Microbes and Environments*, 27,449–455, 2012

[10] Hossain, S., De Silva B., Dahanayake, P. and Heo, G-J., Characterization of virulence properties and multi-drug resistance profiles in motile *Aeromonas* spp. isolated from zebrafish (*Danio rerio*), *Letters in Applied Microbiology*, 67, 598–605, 2018.

[11] Austin, B., Stuckey, L.E., Robertson, P.A.W., Effendi, I. and Griffith, D.R.W., A probiotic strain of *Vibrio alginolyticus* effective in reducing disease caused by *Aeromonas salmonicida*, *Vibrio anguillarum* and *Vibrio ordalli*., *Journal of Fish Disease,* 18, 93–96, 1995.

[12] Moriarty, D.J.W., The role of microorganisms in aquaculture ponds, *Aquaculture*, 151, 333–349, 1997.

[13] Irianto, A. and Austin, B., Probiotics in aquaculture, *Journal of Fish Disease,* 25, 633–642, 2002.

[14] Pérez-Sánchez, T., Ruiz-Zarzuela, I., Blas, I. and Balcázar, J.L., Probiotics in aquaculture: a current assessment, *Reviews in Aquaculture,* 6, 133–146, 2014.

[15] Xia, Y., Lu, M., Chen, G., Cao, J., Gao, F., Wang, M., Liu, Z., Zhang, D., Zhu, H. and Yi, M., Effects of dietary *Lactobacillus rhamnosus* JCM1136 and *Lactococcus lactis* subsp. *lactis* JCM5805 on the growth, intestinal microbiota, morphology, immune response and disease resistance of juvenile Nile tilapia, *Oreochromis niloticus*, *Fish and Shellfish Immunology*, 76, 368–379, 2018.

[16]Abumourad, I.M.K., Abbas, W.T., Awaad, E.S., Authman, M.M.N., El-Shafei, K., Sharaf, O.M., Ibrahim, G.A., Sadek, Z.I. and El-Sayed, H.S., Evaluation of *Lactobacillus plantarum* as a probiotic in aquaculture: emphasis on growth performance and innate immunity, *The Journal of Applied Sciences Research,* 9, 572–582, 2013.

[17] Salminen, S., von Wright, A., Morelli, L., Marteau, P., Brassart, D., de Vos, W.M., Fondén, R., Saxelin, M., Collins, K., Mogensen, G., Birkeland, S.E. and Mattila-Sandholm, T., Demonstration of safety of probiotics–a review, *International Journal of Food Microbiology,* 44, 93–106, 1998

[18] Balcázar, J.L., de Blas, I., Ruiz-Zarzuela, I., Vendrell, D., Gironés, O. and Muzquiz, J.L., Sequencing of variable regions of the 16S rRNA gene for identification of lactic acid bacteria isolated from the intestinal microbiota of healthy salmonids. *Comparative Immunology, Microbiology & Infectious Diseases,* 30, 111–118, 2007.

[19] Mauguin, S. and Novel, G., Characterization of lactic acid bacteria isolated from seafood. *Applied and Environmental Microbiology Journal,* 76, 616–625, 1994.

[20] Sequeiros, C., Vallejo, M., Marguet, E.R. and Olivera, N.L. Inhibitory activity against the fish pathogen *Lactococcus garvieae* produced by *Lactococcus lactis* TW34, a lactic acid bacterium isolated from the intestinal tract of a Patagonian fish, *Archives of Microbiology*, 192, 237–245, 2010.

[21] Nishant, T., Sathish, Kumar, D., Arun Kumar, R., Hima Bindu, K. and Raviteja, Y., Bacteriocin producing probiotic lactic acid bacteria, *Journal of Microbial & Biochemical Technology,* 3, 121–124, 2011.

[22] Kumar, M., Jain, A.K., Ghosh, M. and Ganguli, A., Bacteriocin of *Lactococcus Lactis*. *Journal of Food Safety,* 32, 369–378, 2012.

[23] Messi, P., Bondi, M., Sabia, C., Battini, R. and Manicardi, G., Detection and preliminary characterization of a bacteriocin (plantaricin 35d) produced by a *Lactobacillus plantarum* strain, *International Journal of Food Microbiology*, 64, 193–198, 2001.

[24] Todorov, S. and Dicks, L.M.T., Pediocin ST18, an anti-listerial bacteriocin produced by *Pediococcus pentosaceus* ST18 isolated from boza, a traditional cereal beverage from Bulgaria, *Process Biochemistry,* 40, 365–370, 2005.

[25] Ayeni, F. A., Sánchez, B., Adeniyi, B.A., de Los Reyes-Gavilán, C.G., Margolles, A. and Ruas-Madiedo, P., Evaluation of the functional potential of *Weissella* and *Lactobacillus* isolates obtained from Nigerian traditional fermented foods and cow's intestine, *International Journal of Food Microbiology,* 147, 97–104, 2011.

[26] Jacobsen, C.N., Rosenfeldt, Nielsen, V., Hayford, A.E., Møller, P.L., Michaelsen, K.F., Paerregaard, A., Sandström, B., Tvede, M. and Jakobsen, M., Screening of probiotic activities of forty-seven strains of *Lactobacillus* spp. by *in vitro* techniques and evaluation of the colonization ability of five selected strains in humans, *Applied and Environmental Microbiology*, 65, 4949–4956, 1999.

[27] Zielińska, D., Rzepkowska, A., Radawska, A. and Zieliński, K., *in vitro* screening of selected probiotic properties of *Lactobacillus* strains isolated from traditional fermented cabbage and cucumber, *Current Microbiology*, 70, 183–194, 2015.

[28] Begley, M., Gahan, C.G.M. and Hill, C., The interaction between bacteria and bile, *FEMS Microbiology Reviews*, 29, 625–651, 2005.

[29] Tjørve, K.M.C. and Tjørve, E., The use of Gompertz models in growth analyses, and new Gompertz-model approach: An addition to the Unified-Richards family, *PloS One,* 12, e0178691, 2017.

[30] Hiura, S. Koseki, S. and Koyama, K., Prediction of population behavior of *Listeria monocytogenes* in food using machine learning and a microbial growth and survival database, *Scientific Reports,* 11, 10613, 2021.

[31] Kim, K. and Hong, J.S.A., Hybrid decision tree algorithm for mixed numeric and categorical data in regression analysis, *Pattern Recognition Letters,* 98, 39–45, 2017.

[32] Hajmeer, M., Basheer, I. and Cliver, D.O., Survival curves of *Listeria monocytogenes* in chorizos modeled with artificial neural networks. *Food Microbiology* , 23, 561–570, 2006.

[33] Uzun Yaylacı, E., Yaylacı, M., Ölmez, H. and Birinci, A., Artificial neural network calculations for a receding contact problem, *Computers and Concrete ,* 25, 551–563, 2020.

[34] Yaylacı, M., Eyüboğlu, A., Adıyaman, G., Uzun Yaylacı, E., Öner, E. and Birinci, A., Assessment of different solution methods for receding contact problems in functionally graded layered mediums, *Mechanics of Materials* 154, 103730, 2021.

[35] Trujillo, M.C.R., Alarcon, T.E., Dalmau, O.S. and Ojeda, A.Z., Segmentation of carbon nanotube images through an artificial neural network, *Soft Computing,* 21, 611–625, 2017.

[36] Yan, H., Jiang, Y., Zheng, J., Peng, C. and Li, Q., A multilayer perceptron based medical decision support system for heart disease diagnosis, *Expert Systems With Applications,* 30, 272–81, 2006.

[37] Uzun Yaylacı E., Developing a differentiation technique for the pathogenic bacteria causing disease in sea bass (*Dicentrarchus labrax*) by using artificial neural networks. Doctoral thesis, Karadeniz Technical University, The Graduate School of Natural and Applied Sciences, Trabzon, Turkey, 47p., 2019

[38] Jarvis, B., Statistical aspects of the microbiological analysis of foods. Elsevier, Amsterdam, 1989

[39] Panagou, E.Z., Tassou, C.C., Saravanos, E.K. and Nychas, G.J., Application of neural networks to simulate the growth profile of lactic acid bacteria in green olive fermentation. *Journal of Food Protection,* 70, 1909–1916, 2007.

[40] Fath, A.H., Madanifar, F. and Abbasi, M., Implementation of multilayer perceptron (MLP) and radial basis function (RBF) neural networks to predict solution gas-oil ratio of crude oil systems, *Petroleum,* 6, 80–91, 2020.

[41] Cakiroglu, E., Comez, I. and Erdol, R., Application of artificial neural network to double receding contact problem with a rigid stamp, *Structural Engineering and Mechanics,* 21, 205–220, 2005.

[42] Yu, H., Xie, T., Paszczynski, S. and Wilamowski, B., Advantages of Radial Basis Function Networks for Dynamic System Design, *IEEE Transactions on Industrial Electronics,* 58, 5438–5450, 2011.

[43] Bayram, S., Ocal, M., E., Laptali, Oral, E. and Atis, C.D., Comparison of multi-layer perceptron (MLP) and radial basis function (RBF) for construction cost estimation: the case of Turkey, *The Journal of Civil Engineering and Management,* 22, 480–490, 2016.

[44] Wawrzyniak, J., Application of artificial neural networks to assess the mycological state of bulk stored rapeseeds, *Agriculture,* 10, 567, 2020.

[45] Kumar, A., Kundu, S. and Debnath, M., Effects of the probiotics *Lactococcus lacttis* (MTCC-440) on *Salmonella enteric* serovar Typhi in co-culture study, *Microbial Pathogenesis,* 120, 42–46, 2018.

[46] Vaseeharan, B. and Ramasamy, P., Control of pathogenic *Vibrio* spp. by *Bacillus subtilis* BT23, a possible probiotic treatment for black tiger shrimp *Penaeus monodon*, *Letters in Applied Microbiology,* 36, 83–87, 2003.

[47] Eren, B. and Eyüpoğlu, V., Modelling of recovery efficiency of Ni(II) ion using artificial neural network, in 6th International Advanced Tech-nologies Symposium (IATS'11), 16–18 May 2011, Elazığ, Turkey.

[48] Kayadelen, C., Taşkıran, T., Günaydın, O. and Fener, M., Adaptive neuro-fuzzy modeling for the swelling potential of compacted soils, *Environmental Earth Sciences,* 59, 109–115, 2009.

[49] Orhan, U., Hekim, M. and Ozer, M., EEG signals classification using the K-means clustering and a multilayer perceptron neural network model, *Expert Systems With Applications*, 38, 13475–13481, 2011.

[50] Le, Cun, Y., Denker, J.S. and Solla, S.A., Optimal brain damage, *Advances in Neural Information Processing Systems,* 2, 598–605, 1990.